Synthesis and Dual-Mode Electrochromism of Anisotropic Monoclinic Nb$_{12}$O$_{29}$ Colloidal Nanoplatelets

Hsin-Che Lu, Sandeep Ghosh,[§] Naman Katyal,[§] Vikram S. Lakhanpal, Ioana R. Gearba-Dolocan, Graeme Henkelman, and Delia J. Milliron*

Read Online

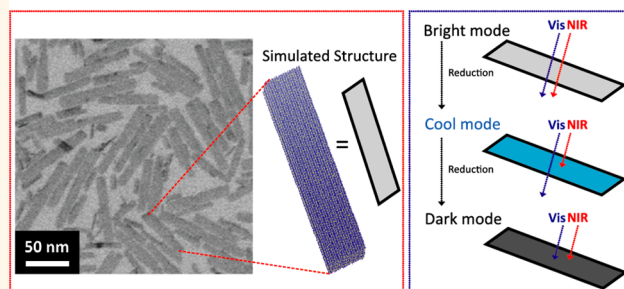ACCESS | Metrics & More | Article Recommendations | Supporting Information

ABSTRACT: Transition metal oxide nanocrystals with dual-mode electrochromism hold promise for smart windows enabling spectrally selective solar modulation. We have developed the colloidal synthesis of anisotropic monoclinic Nb$_{12}$O$_{29}$ nanoplatelets (NPLs) to investigate the dual-mode electrochromism of niobium oxide nanocrystals. The precursor for synthesizing NPLs was prepared by mixing NbCl$_5$ and oleic acid to form a complex that was subsequently heated to form an oxide-like structure capped by oleic acid, denoted as niobium oxo cluster. By initiating the synthesis using niobium oxo clusters, preferred growth of NPLs over other polymorphs was observed. The structure of the synthesized NPLs was examined by X-ray diffraction in conjunction with simulations, revealing that the NPLs are monolayer monoclinic Nb$_{12}$O$_{29}$, thin in the [100] direction and extended along the *b* and *c* directions. Besides having monolayer thickness, NPLs show decreased intensity of Raman signal from Nb−O bonds with higher bond order when compared to bulk monoclinic Nb$_{12}$O$_{29}$, as interpreted by calculations. Progressive electrochemical reduction of NPL films led to absorbance in the near-infrared region (stage 1) followed by absorbance in both the visible and near-infrared regions (stage 2), thus exhibiting dual-mode electrochromism. The mechanisms underlying these two processes were distinguished electrochemically by cyclic voltammetry to determine the extent to which ion intercalation limits the kinetics, and by verifying the presence of localized electrons following ion intercalation using X-ray photoelectron spectroscopy. Both results support that the near-infrared absorption results from capacitive charging, and the onset of visible absorption in the second stage is caused by ion intercalation.

KEYWORDS: *metal oxides, niobium oxides, electrochromism, colloidal synthesis, smart windows, nanocrystals, 2d materials*

Electrochromic smart windows electrochemically modulate transmittance of sunlight to improve indoor energy management.[1,2] Conventional electrochromics based on transition metal oxide films have attained limited success due in part to slow switching kinetics and poor spectral control.[1,2] To obtain more refined spectral control, recent reports have advanced the strategy of using transition metal oxide nanocrystals (NCs) that can accommodate electrochemical charge through both intercalation and capacitive charging, the latter producing delocalized electrons with distinct optical absorption. Based on this mechanism, these NCs are able to selectively modulate near-infrared (NIR) light by capacitive charging and visible light by the traditional ion intercalation mechanism.[3−6] Despite this advantage, issues surrounding efficiency and electrochemical and optical instabilities in NCs need to be addressed to facilitate wide adoption.[7,8]

Niobium(V) oxides (Nb$_2$O$_{5−x}$) display rich polymorphic forms with diverse electronic and optical properties.[9,10] In particular, the electrochemical reduction of Nb^{5+} to Nb^{4+} following Li$^+$ ion intercalation and the concomitant optical response has motivated investigation of electrochromic properties.[11−13] Films of bulk, crystalline Nb$_2$O$_{5−x}$ are electrochemically and photochemically stable owing to the minimal structural changes that occur during Li$^+$ ion intercalation and a large electronic band gap,[14,15] yet
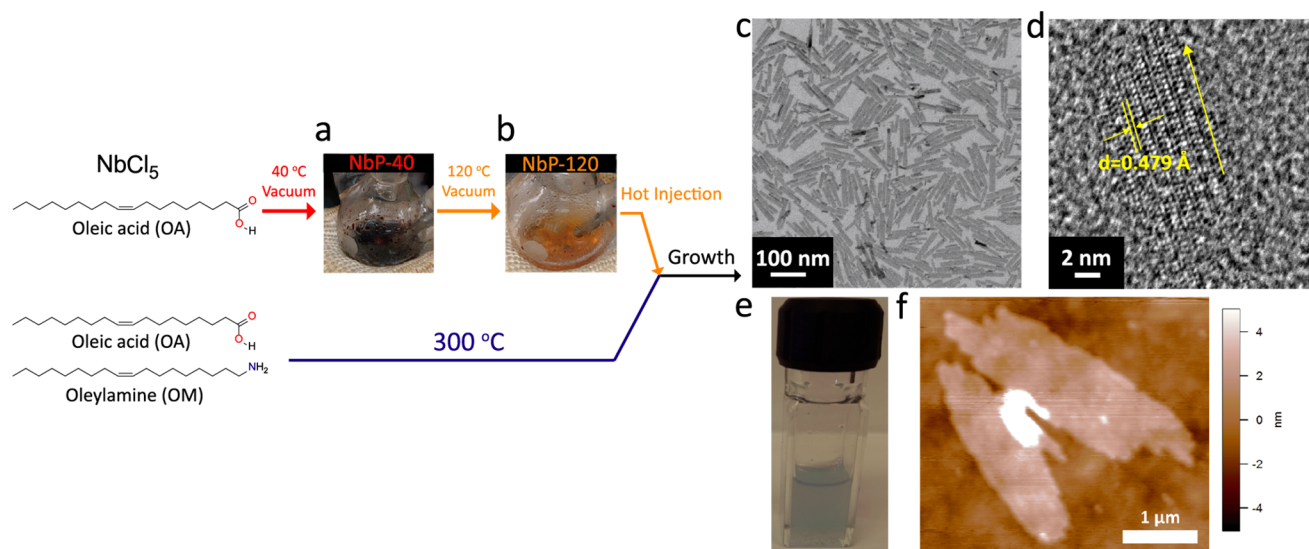
Figure 1. Scheme of synthesis producing NPLs. Niobium precursor was prepared by mixing $NbCl_5$ and OA, then (a) heated to 40 °C under vacuum to reach the first stage with blood-red color (NbP-40) and (b) further heated to 120 °C under vacuum to reach the second stage with orange color (NbP-120). Morphological characterization of NPLs using (c) bright-field STEM imaging and (d) HRTEM imaging. In (d), the yellow arrow corresponds to the elongated direction of the NPL (also the *b* axis of monoclinic $Nb_{12}O_{29}$), and the *d*-spacing corresponds to the (004) plane of monoclinic $Nb_{12}O_{29}$. (e) Photograph of NPL dispersion in toluene. (f) AFM topographic image of NPLs to demonstrate their thickness.

electrochromic spectral control has not been reported. In the most studied pseudohexagonal phase, these films absorb light broadly across the visible and NIR regions in their reduced state.[11] Among Nb_2O_{5-x} crystals, there are a variety of monoclinic phase polymorphs, with Nb_2O_5 being the most oxidized form and $Nb_{12}O_{29}$ being the most reduced form.[16] The crystal structure of monoclinic $Nb_{12}O_{29}$ (Figure S1) contains vertex-sharing niobium oxygen octahedra (NbO_6 octahedra) arranged in blocks that share edges with NbO_6 octahedra in other blocks in an adjacent crystalline layer.[17] In monoclinic $Nb_{12}O_{29}$, the additional electrons owing to oxygen deficiency populate the conduction band, giving rise to metallic conduction and antiferromagnetic order.[16,18] Additionally, monoclinic $Nb_{12}O_{29}$ exhibits a wide band gap and reversible electrochemical cycling of Li^+ ions without structural changes, suggesting it could be a stable electrochromic coating material.[18,19] With this motivation, we demonstrate the synthesis of monoclinic $Nb_{12}O_{29}$ NCs and their use in electrochromic coatings. We utilize their potential for accommodating delocalized electrons during capacitive charging, and for Nb^{5+} reduction following Li^+ ion intercalation, inducing dual-mode electrochromism. These nanoscale crystals exhibit the stability anticipated based on the properties of the bulk crystalline phase.

Crystalline Nb_2O_{5-x} has been prepared by sol−gel,[20] solvothermal,[21,22] and vapor deposition methods.[11,23] However, the reported route for making monoclinic $Nb_{12}O_{29}$ involves first synthesizing monoclinic Nb_2O_5 at high temperature (~1100 K) and then reducing it in the presence of niobium metal, at similarly high temperature.[16,24] This route is energy intensive and yields only bulk crystals of monoclinic $Nb_{12}O_{29}$. As an alternative, colloidal synthesis, featuring direct crystallization of metal ion sources in solvents at moderate temperature, has met great success in producing metal oxide NCs with tight control over their size, stoichiometry, morphology, and crystal phase.[25] In this research, we sought

to develop the colloidal synthesis of monoclinic $Nb_{12}O_{29}$ NCs and to investigate their electrochromic properties.

Herein, we report the colloidal synthesis of monoclinic $Nb_{12}O_{29}$ NCs with two-dimensional morphology (nanoplatelets, NPLs). By preparing niobium oxo clusters as a synthesis precursor, preferred growth of monoclinic-phase NPLs over orthorhombic Nb_2O_5 nanorods (NRs) was observed. The precursor formation chemistry was investigated, revealing the formation of niobium chloro oleate upon mixing $NbCl_5$ and oleic acid (OA)[26] and that subsequent heating cleaves the Nb−Cl bonds to form niobium oxo clusters, which eventually leads to selective growth of NPLs as observed in reaction aliquots. X-ray diffraction (XRD) analysis in conjunction with simulations indicates that the NPLs are monolayers of monoclinic $Nb_{12}O_{29}$. In Raman spectroscopy analysis, the NPLs show decreased intensity of vibrations of Nb−O bonds with higher bond order, which can be ascribed to their monolayer thickness as suggested by calculated spectra.

Upon reducing in a Li-based electrolyte, NPL films absorb NIR light at moderate potential, and absorb both NIR and visible light at more reducing potential, thus achieving selective control of solar spectrum transmittance. These two electrochromic processes were distinguished by the presence of localized electrons following electrochemical charging based on *ex situ* X-ray photoelectron spectroscopy (XPS) analysis together with observations of electrochemical kinetics using variable rate cyclic voltammetry. The presence of localized electrons, indicated by the reduction of Nb^{5+} to Nb^{4+}, is understood to result from Li^+ ion intercalation. In analyzing the electrochemical kinetics, ion intercalation into the crystal lattice was associated with ion diffusion using the *b*-value test, a method used to estimate the extent to which the electrochemical reaction is limited by ion diffusion. Overall, the chemical and electrochemical evidence support that visible absorption arises due to Li^+ ion intercalation, and the NIR absorption results from capacitive charging.
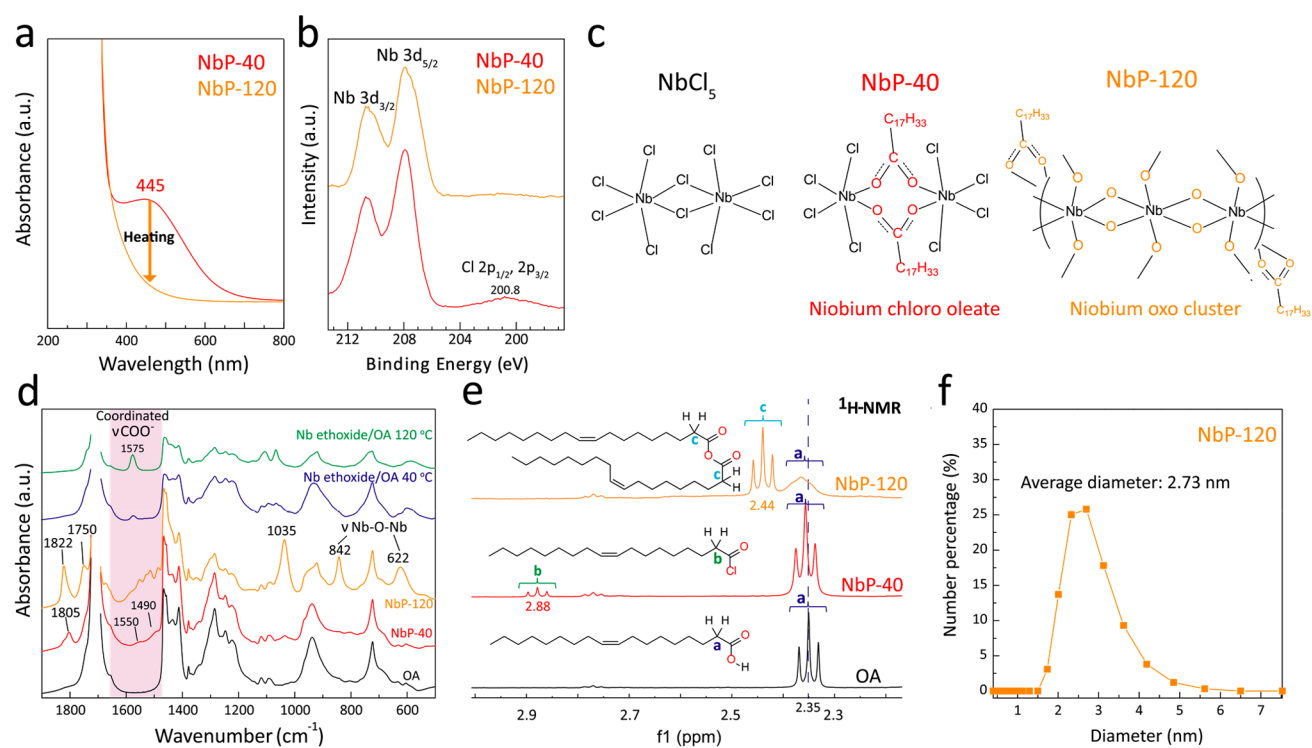
Figure 2. Spectroscopic characterization of NbP-40 (red), NbP-120 (orange), OA (black), and a niobium ethoxide/OA mixture at 40 °C (blue) and 120 °C (green). (a) UV−vis−NIR spectra showing the elimination of LMCT absorption. (b) XPS spectra showing the signal of Cl⁻ ions. (c) Proposed structures of NbCl₅, NbP-40 (niobium chloro oleate), and NbP-120 (niobium oxo cluster). (d) Fourier Transform infrared (FTIR) spectra showing the coordinated COO⁻ stretches, stretches of Nb−O−Nb bonds, and peaks from oleoyl chloride (1805 cm⁻¹) and oleic anhydride (1035, 1750, and 1822 cm⁻¹). (e) ¹H NMR spectra showing signals from OA (2.35 ppm), oleoyl chloride (2.88 ppm), and oleic anhydride (2.44 ppm) along with their structures. (f) DLS particle diameter distribution of NbP-120.

RESULTS AND DISCUSSION

Synthesis and Morphological Characterization. Colloidal synthesis of NPLs involves the injection of prepared niobium precursor into a hot bath composed of OA and oleylamine (OM) to initiate growth (details in the Methods section), as illustrated in Figure 1. Upon mixing NbCl₅ and OA in the precursor preparation step, immediate formation of a blood-red solution was observed, and its appearance remained the same when heated to 40 °C under vacuum to yield a homogeneous solution (NbP-40, shown in Figure 1a). Further heating NbP-40 to 120 °C under vacuum resulted in a color change from blood-red to orange (NbP-120, shown in Figure 1b). NCs were synthesized by injecting NbP-120 into a hot bath of OA and OM at 300 °C and allowing the reaction to proceed for 10 min, leading to formation of a cloudy suspension, indicating crystal growth. After purification, the products were imaged using scanning transmission electron microscopy (STEM), revealing a two-dimensional nano-platelet-like morphology (Figure 1c), referred to as NPLs for further discussion. In high-resolution transmission electron microscopy (HRTEM) imaging (Figure 1d), the atomic arrangement in the NPLs appears as a structural-column arrangement with boundaries between each column. A *d*-spacing of 4.79 Å can be measured in the short axis direction of the NPL in Figure 1d and is consistent with the spacing determined from the fast Fourier transform (FFT) of the HRTEM image (Figure S2). Similar structures have also been observed in the cases of bulk monoclinic Nb₂O₅₋ₓ crystals (Nb₂O₅ and Nb₁₂O₂₉).[27,28] The dispersion of NPLs in toluene exhibits a blue color (Figure 1e). Size distribution histograms

obtained by STEM imaging show that the NPLs have an average length of 95.2 ± 32.5 nm along the long axis and an average width of 9.4 ± 2.7 nm perpendicular to the long axis (Figure S3). An atomic force microscopy (AFM) topographic image of an island of NPLs was collected to evaluate their thickness (Figure 1f). A very thin thickness of approximately 2.7 nm was measured based on the height profile of this AFM image (Figure S4), indicating that the NPLs could be monolayer materials of niobium oxide. This possibility was further examined and confirmed by XRD analysis, as discussed below. The NPL samples after removing the surface ligands have a smaller approximated thickness of 1.7 nm measured by AFM imaging (Figure S5), which again suggests the monolayer thickness of NPLs.

In contrast with the NPLs synthesized from the NbP-120 precursor, injecting NbP-40 using the same reaction conditions resulted in a mixture of a small amount of NPLs and a main product that has a nanorod-like morphology (Figure S6). We hypothesize that these nanorod-like products are orthorhombic Nb₂O₅ NRs, like those recently reported.[26] Following the protocol in this previous study,[26] directly heating NbP-40 along with solvents reproduced pure NRs, as shown in Figure S6.

Precursor Characterization and Synthetic Mechanism. As discussed, initiating NC growth in the same reaction environment, but with different niobium precursors, leads to NCs with different morphologies. Hence, the niobium precursors, NbP-40 and NbP-120, were probed by different spectroscopic techniques to investigate their composition and influence on the synthetic result. By ultraviolet−visible−near-
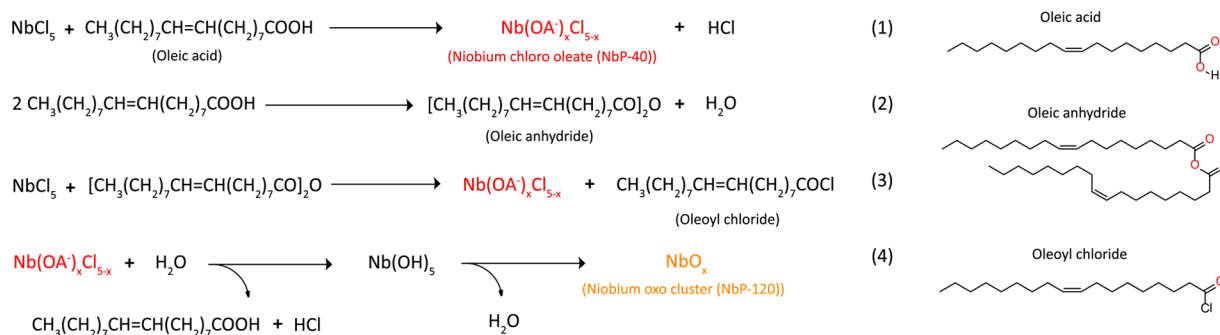
Figure 3. Proposed mechanism accounting for the formation of niobium chloro oleate upon mixing $NbCl_5$ and OA (eq 1), oleic anhydride as a product from the condensation of OA (eq 2), oleoyl chloride from the reaction between $NbCl_5$ and oleic anhydride (eq 3), and niobium oxo cluster from hydrolysis (eq 4).

infrared (UV−vis−NIR) spectroscopy (Figure 2a), we identified that the blood-red color of NbP-40 is due to an absorption band in the visible region with a peak centered at 445 nm, while converting the NbP-40 to NbP-120 by heating eliminates this absorption feature. We hypothesize that the distinctive absorption in NbP-40 is due to ligand to metal charge transfer (LMCT) absorption occurring from the electrons in the carboxylate groups of metal-bound OA molecules to the empty d orbitals of Nb^{5+} ions. Therefore, NbP-40 is understood to be a complex of both Cl^- ions and deprotonated OA molecules coordinating to Nb^{5+} ions, named as niobium chloro oleate ($Nb(OA)_xCl_{5-x}$). A similar complex was reportedly formed by mixing $NbCl_5$ and acetic acid to form niobium chloro carboxylate, with one carboxylate ion coordinating to two Nb^{5+} ions in a bridging configuration.[29] Upon converting the NbP-40 to NbP-120, we hypothesize that the quenching of LMCT absorption is due to the conversion from a complex-like composition to an oxide-like composition, consistent with NbP-120 having absorption residing largely in the UV region. NbP-120, behaving similarly to an oxide, is referred to as a niobium oxo cluster for the remaining discussion.

The elemental compositions of NbP-40 and NbP-120 were studied by X-ray photoelectron spectroscopy (XPS) to investigate the possible presence of Cl^- ions (Figure 2b). After washing with acetone to remove OA and drying, signal from Cl $2p_{1/2}$ and $2p_{3/2}$, forming a broad band centered at 200.8 eV, can be observed in NbP-40, but not in NbP-120. This result indicates the removal of Cl^- ions during the conversion from NbP-40 to NbP-120, aligning with our hypothesis that NbP-120 forms an oxide structure and Nb−Cl bonds are cleaved. Additionally, it was reported that $NbCl_5$ contains Cl^- ions in two distinct bonding environments, one forming a bridging coordination between two Nb^{5+} ions, and the other forming a nonbridging coordination to a single Nb^{5+} ion, as illustrated in Figure 2c. In XPS spectra, these two can be distinguished by Cl $2p_{3/2}$ peaks at 199.6 and 200.6 eV, respectively.[30] This evidence suggests the Cl^- ions in NbP-40 are present mostly in nonbridging coordination according to the peak position, with the bridging Cl^- ions being replaced by $RCOO^-$ ions.

IR and ^1H NMR spectroscopies were applied to investigate the structure of the niobium precursors. The IR spectrum of NbP-120 has peaks at 622 and 842 cm^{-1} that can be assigned to the stretches of Nb−O−Nb bridging and collinear bonds, respectively (Figure 2d).[31] Moreover, multiple peaks (1485, 1515, 1530, 1550, and 1580 cm^{-1}) appear in the region (from

1480 to 1650 cm^{-1}) corresponding to the stretches of coordinated COO^- bonds.[32−35] These results highlight the fact that NbP-120 has an oxide-like structure with abundant Nb−O−Nb bonds and COO^- ions coordinating on the oxide surface. In the ^1H NMR spectrum of OA (Figure 2e), the protons on the α carbon of OA molecules exhibit triplet resonance centered at 2.35 ppm, while the spectrum of NbP-120 shows broadened triplet resonance and downfield chemical shift for this resonance, indicating that the COO^- ions are tightly bound on the oxide surface,[36] aligning with the interpretation of the IR spectrum. On the other hand, the IR spectrum of NbP-40 (Figure 2d) has weak peaks at 1490 and 1550 cm^{-1} assigned to stretching modes of bridging COO^- ions.[29] As for the ^1H NMR spectrum of NbP-40 (Figure 2e), only a slight broadening and downfield shift can be observed for the triplet at 2.35 ppm, suggesting OA is still mostly noncoordinating. The structures of NbP-40 and NbP-120 are proposed in Figure 2c, in which NbP-40 is a complex of niobium chloro oleate with $RCOO^-$ ions coordinating in the bridging position, and NbP-120 is a niobium oxo cluster compound with $RCOO^-$ ions coordinating on the surface. Dynamic light scattering (DLS) was used to confirm the presence of niobium oxo clusters in NbP-120, indicating an average hydrodynamic particle diameter of 2.73 nm (Figure 2f). In contrast, no appreciable signal was measured for NbP-40, consistent with a smaller, molecular structure.

Having deduced the structures of NbP-40 and NbP-120, we now focus on the mechanisms leading to formation of these two precursors. It was reported that niobium chloro carboxylate will react with acid anhydride to form acyl chloride.[29] In our reaction environment, the analogues would be oleic anhydride and oleoyl chloride. In the IR and ^1H NMR spectra of NbP-40 (Figure 2d and e), the C=O stretch (1802 cm^{-1}) and triplet resonance at 2.88 ppm can be assigned to oleoyl chloride.[37] In the case of NbP-120, peaks from the C−O−C stretch (1035 cm^{-1}), C=O symmetric and asymmetric stretches (1750 and 1822 cm^{-1}), and triplet resonance at 2.44 ppm can be assigned to oleic anhydride.[37] A mechanism accounting for the formation of NbP-40 and NbP-120 is proposed in Figure 3. Niobium chloro oleate forms upon mixing $NbCl_5$ and OA at 40 °C (Figure 3, eq 1).[29] At the same time, a small amount of OA condenses into oleic anhydride with water as byproduct (Figure 3, eq 2), and subsequently, oleic anhydride reacts with the remaining $NbCl_5$ to form oleoyl chloride and niobium chloro oleate (Figure 3, eq 3), as suggested in the literature.[29] Heating to 120 °C further drives reaction 2 to generate more water that reacts with niobium
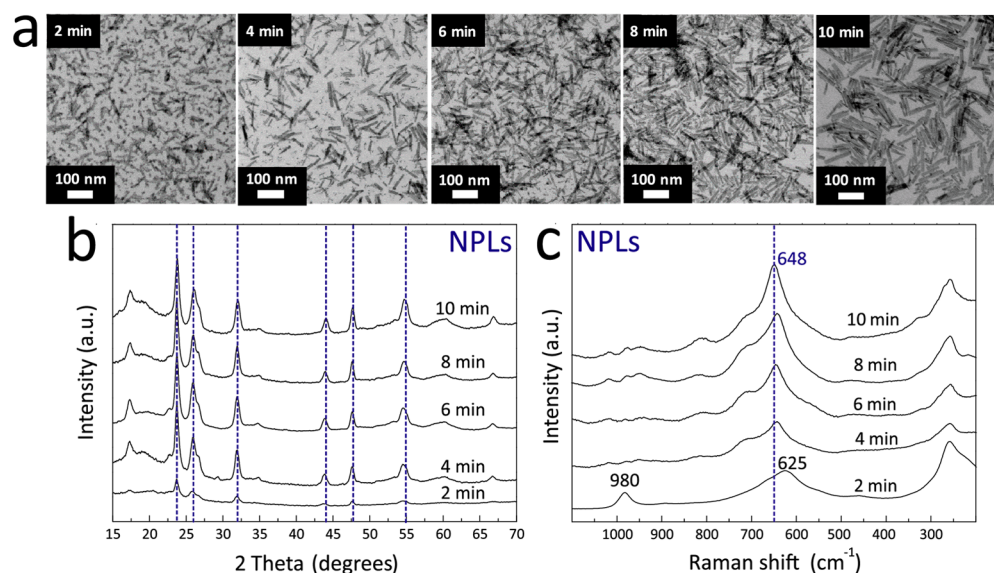
Figure 4. Characterization of aliquots during the injection synthesis of NPLs. Blue dash lines correspond to the characteristic peaks of NPLs. (a) STEM images showing clusters and fragmented NPLs initially (2 min) and growing into NPLs in the end. (b) Experimental XRD patterns showing amorphous signature initially (2 min) and signals from NPLs in the end. (c) Experimental Raman spectra showing amorphous signature initially (2 min) and signals from NPLs in the end.

chloro oleate *via* hydrolysis to form niobium oxo clusters (Figure 3, eq 4).[25] According to this mechanism, oleic anhydride will remain in NbP-120 as a byproduct, consistent with our FTIR analysis (Figure 2d). To verify the role of Cl⁻ ions in the proposed mechanism, we prepared precursors based on niobium ethoxide and OA, which were mixed and then heated to 40 and 120 °C under vacuum. A new IR peak at 1575 cm⁻¹ arises when heating niobium ethoxide and OA to 120 °C, suggesting coordination may occur. However, no IR bands from oleic anhydride or oleoyl chloride were observed (Figure 2d), indicating the reaction does not follow the same scheme as when using $NbCl_5$ as the niobium source. We propose that $NbCl_5$ catalyzes the reaction forming oleic anhydride (eq 2), thus enabling the subsequent oxo cluster formation.

With the composition and formation mechanism of NbP-40 and NbP-120 described, we now examine how the precursor chemistry affects NC growth. In past reports, growth of Nb_2O_{5-x} crystals with NR morphology was often accomplished using $NbCl_5$ as the niobium source,[21,38,39] suggesting that Cl⁻ ions may play a role in regulating crystal growth or even controlling faceting.[40,41] Our previous study detailed the mechanism leading to the growth of orthorhombic Nb_2O_5 NRs in a colloidal reaction starting from $NbCl_5$.[26] In brief, the precursor of niobium chloro oleate reacts to form clusters at lower temperatures. Upon further heating crystallization occurs, preferentially forming NRs. In this research, we selectively synthesize two precursors, niobium chloro oleate (NbP-40) and niobium oxo cluster (NbP-120), and initiate colloidal crystal growth using them at designated temperature by hot injection.

The mechanism of crystal growth was investigated by tracking the reaction progression using aliquots every 2 min after injection, as shown in Figure 4 for injecting NbP-120 and Figure S7 for injecting NbP-40. In the STEM imaging of aliquots produced during the synthesis employing NbP-120, small clusters and fragmented NPLs were observed initially (Figure 4a). As the reaction progresses, these clusters gradually

decompose and deposit on the fragmented NPLs, leading to the final NPL products. On the other hand, following injection of NbP-40, a mixture of mostly NRs and a small amount of NPLs was observed throughout the aliquots (Figure S7), highlighting the fact that initiating the synthesis using niobium chloro oleate favors the growth of NRs. Synthesis progression was also tracked by XRD patterns and Raman spectra as a complement to the STEM imaging, with details being discussed more thoroughly in the structure characterization section, while the basic results are discussed here.

For the synthesis initiated by injecting NbP-120, the XRD patterns (Figure 4b) show weak signals from NPLs at 2 min after injection due to the occurrence of mixed amorphous clusters and fragmented NPLs, while the other patterns show clear signals from NPLs. When synthesis is performed by injecting NbP-40, the XRD patterns (Figure S7) show signatures from both NRs and NPLs with signals from NPLs gradually increasing in relative intensity. In the Raman spectra of products resulting from the injection of NbP-120 (Figure 4c) broadened peaks at 625 and 980 cm⁻¹ are observed for a 2 min reaction time that eventually evolve into a spectrum with the signatures of NPLs. The broadened feature around 625 cm⁻¹ can be assigned to the stretch of the Nb−O−Nb bond of the amorphous niobium oxo cluster present in the initial stage.[42,43] The peak at 980 cm⁻¹ can be assigned to terminal Nb=O bonds also from the cluster.[44] For the reaction done by injecting NbP-40, a strong Raman peak at 710 cm⁻¹ arose immediately and was observed throughout the aliquots (Figure S7), corresponding to NRs, while a weak peak at 648 cm⁻¹ grew in gradually during the reaction, corresponding to NPLs.

On the basis of these observations, we concluded that when injecting NbP-120, the niobium oxo clusters serve as amorphous seeds that eventually grow into NPLs, while the injection of NbP-40 results in a mixture of mostly NRs. While the previously reported heat-up strategy for colloidal niobium oxide synthesis favored NRs, we find that deliberate synthesizing and injection of a niobium oxo cluster precursor tunes the
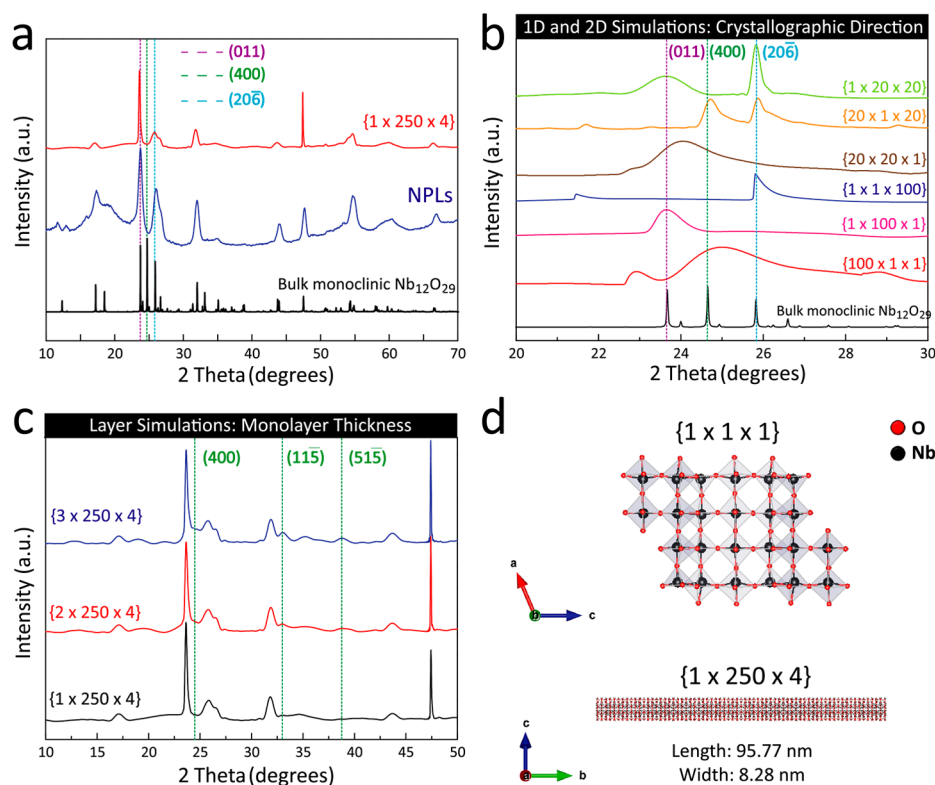
Figure 5. Structural characterization of NPLs using experimental and simulated XRD patterns. (a) Experimental pattern of NPLs (blue), reference of bulk monoclinic $Nb_{12}O_{29}$ crystals (black), and optimized simulated pattern using a $\{1 \times 250 \times 4\}$ supercell (red). (b) Simulated patterns using $\{100 \times 1 \times 1\}$ (red), $\{1 \times 100 \times 1\}$ (pink), $\{1 \times 1 \times 100\}$ (blue), $\{20 \times 20 \times 1\}$ (brown), $\{20 \times 1 \times 20\}$ (orange), and $\{1 \times 20 \times 20\}$ (yellow-green) supercells. (c) Simulated patterns of $\{1 \times 250 \times 4\}$ (black), $\{2 \times 250 \times 4\}$ (red), and $\{3 \times 250 \times 4\}$ (blue) supercells. (d) Atomic models of a $\{1 \times 1 \times 1\}$ unit cell and a $\{1 \times 250 \times 4\}$ supercell with lateral size matching the NPLs.

crystallization mechanism to favor the growth of crystals with NPL morphology.

Structural Characterization by X-ray Diffraction. The XRD pattern of the synthesized NPLs compares favorably to the reference pattern of bulk monoclinic $Nb_{12}O_{29}$ crystals (PDF#01-073-1610, Figure 5a). The pattern of the NPLs shares the (011) and (20$\bar{6}$) reflections with the bulk reference, while missing the main reflection from (400) planes at $2\theta = 24.6°$. For comparison, the experimental pattern of NRs (Figure S8) shows only the reflections from the (001) planes of the orthorhombic Nb_2O_5 crystal structure (PDF#00-030-0873), and the pattern of an NR and NPL mixture resulting from synthesis with NbP-40 (Figure S8) shows signatures of both the materials, verifying that the NRs present in these two cases share the same structure.

To investigate the missing reflection in the pattern of the NPLs, simulations of XRD patterns were performed based on the Debye scattering formula, in which the intensity of the incident X-rays being scattered by every pair of ions within a finite crystal is calculated.[45] Simulations were performed by calculating the scattering intensity from supercells based on the unit cell of monoclinic $Nb_{12}O_{29}$ repeated different numbers of times in each crystallographic direction, indicated as $\{a \times b \times c\}$. Details of the simulations are discussed in the Methods section. Examples of this simulation method are shown in Figure S8, demonstrating the results produced by using crystal sizes ranging from the $\{1 \times 1 \times 1\}$ unit cell to the $\{10 \times 10 \times 10\}$ supercell. In the smallest system, the $\{1 \times 1 \times 1\}$ cell, all reflections are broad and nondescript. By contrast, the pattern of the $\{10 \times 10 \times 10\}$ supercell shows reflections with distinct

peaks. The broadened reflections in small cells arise because in finite crystals insufficient scattering intensity is generated due to a finite number of ions to create strong constructive interference, thus resulting in weak or absent reflections in their XRD patterns.[46]

We hypothesize that the absence of the (400) reflection in the XRD pattern of the NPLs is due to insufficient ions presenting in a specific crystallographic direction. To verify this, we explored how well the pattern of NPLs could be reproduced by simulating diffraction from finite crystals consisting of cells of monoclinic $Nb_{12}O_{29}$ repeated various times in different crystallographic directions. The simulation result that is most similar to the experimental pattern uses the $\{1 \times 250 \times 4\}$ supercell shown in Figure 5a. The simulated pattern matches all the reflections in the experimental pattern of the NPLs. The morphology of the $\{1 \times 250 \times 4\}$ supercell, corresponding to the simulated structure of an NPL, is a monolayer of monoclinic $Nb_{12}O_{29}$ in the [100] direction elongated two-dimensionally along the b and c axes. In addition, in Figure 1d, a d-spacing of 4.79 Å along the short axis of NPLs corresponds to the (004) plane of monoclinic $Nb_{12}O_{29}$, indicating that the growth direction, perpendicular to the short axis, is along the b axis of monoclinic $Nb_{12}O_{29}$. Our process for obtaining the $\{1 \times 250 \times 4\}$ supercell as the best representation of the NPLs involved simulations varying both crystallographic orientation and layer thickness (Figure 5b and c, respectively). Simulations using supercells extended in one or in two dimensions are shown in Figure 5b. In the simulations of one-dimensional structures ($\{100 \times 1 \times 1\}$, $\{1 \times 100 \times 1\}$, and $\{1 \times 1 \times 100\}$ supercells), we found that
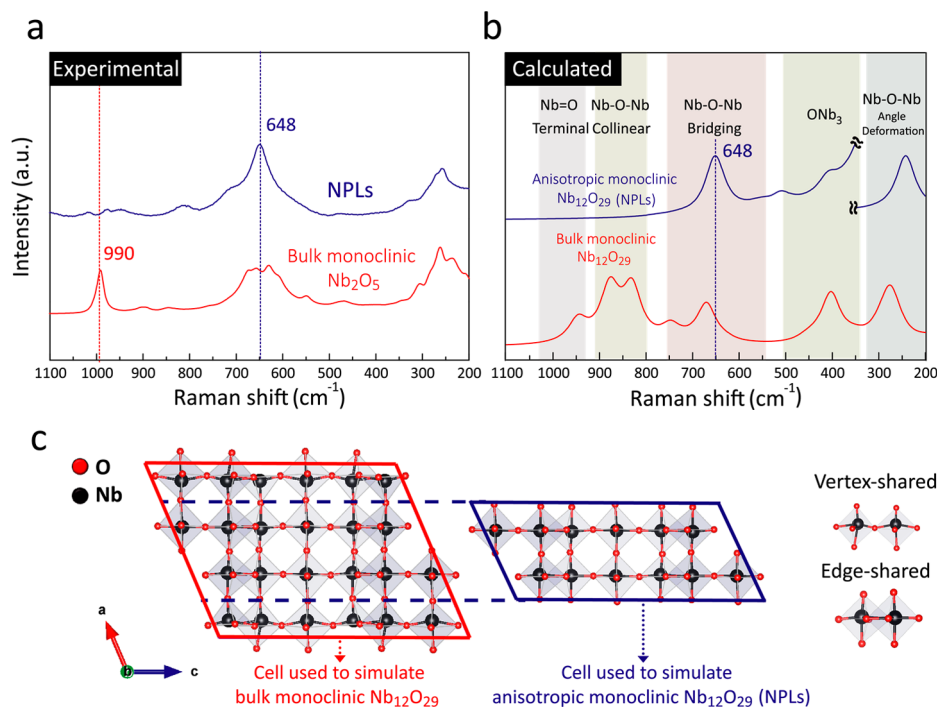
Figure 6. Experimental and calculated Raman spectra. (a) Experimental spectra of NPLs (blue) and bulk monoclinic Nb_2O_5 crystals (red). (b) Calculated spectra of bulk monoclinic $Nb_{12}O_{29}$ crystals (red) and anisotropic monoclinic $Nb_{12}O_{29}$ crystals (blue), or equivalently the NPLs, using the cells shown in (c). In (c), the red cell is the unit cell of monoclinic $Nb_{12}O_{29}$. The blue cell was made by stripping away the ions from 0 to 0.33 and 0.66 to 1.00, in terms of the unit cell parameter, along the [100] direction (or a axis) in the unit cell of monoclinic $Nb_{12}O_{29}$.

the (400) reflection, the one missing in the experimental pattern, is present only in the pattern of the $\{100 \times 1 \times 1\}$ supercell, suggesting that elongation along the [100] direction is absent in NPLs. In two-dimensional structures ($\{20 \times 20 \times 1\}$, $\{20 \times 1 \times 20\}$, and $\{1 \times 20 \times 20\}$ supercells), we observe that the (400) reflection is only suppressed in the $\{1 \times 20 \times 20\}$ supercell, suggesting that the NPLs are elongated in the b and c crystallographic directions since the (400) reflection is not observed in their XRD pattern.

Having assigned the missing crystallographic direction of NPLs, we performed simulations of $\{1 \times 250 \times 4\}$, $\{2 \times 250 \times 4\}$, and $\{3 \times 250 \times 4\}$ supercells to simulate the effect of layer thickness in the [100] direction. The lateral size of these structures was chosen to closely match the averaged values obtained from STEM imaging, that is, 95.2 nm in length and 9.4 nm in width in STEM imaging and 95.77 nm in length and 8.28 nm in width in simulations. As the number of layers in the [100] direction increases, (400), (11), and (51) reflections arise (Figure 5c), which is not observed in the experimental pattern of the NPLs. A magnified view for comparing the experimental pattern to the simulated patterns in Figure 5c is presented in Figure S9. As mentioned previously, the thickness of NPLs was measured as approximately 2.7 nm using AFM. According to the above simulations, since the thickness of the NPLs is along the a axis, along which the unit cell has a lattice constant of 1.568 nm, and taking the oleic acid ligand on the ligand-capped NPL surface into account, we concluded that the measured thickness of NPLs comprises a single unit cell of monoclinic $Nb_{12}O_{29}$ in the [100] direction along with one layer of oleic acid ligand. Additionally, the thickness of ligand-stripped NPLs has an average value of 1.7 nm, which is in good agreement with the theoretical thickness of 1.568 nm. Both physical characterization and the XRD simulations lead us to

conclude that the NPLs are monolayer monoclinic $Nb_{12}O_{29}$ in the [100] direction.

The resulting atomistic model of the $\{1 \times 250 \times 4\}$ supercell used in simulations, which is the best representation of the NPL structure, is shown in Figure 5d together with the $\{1 \times 1 \times 1\}$ unit cell. The very thin structural dimensions in the [100] direction result in the suppression of the (400) reflection seen experimentally and reproduced in simulations based on the Debye scattering formula using finite crystals. In metal oxides, suppressed reflection due to their thin thickness is often discussed in exfoliating and self-assembly synthetic methods, both of which produce two-dimensional crystals with lateral size ranging from nanoscale to micron scale.[47,48] Our method for making monoclinic $Nb_{12}O_{29}$ NPLs shares similarities with the self-assembly approach, both starting from metal ionic sources in a bottom-up synthesis, but NPLs have much smaller and more uniform lateral dimensions.[49] In contrast with other colloidal metal oxide NCs, anisotropic growth of NCs along a specific crystallographic direction has been reported in the cases of tungsten oxide NPLs and titanium oxide NRs;[32,50] however, a two-dimensional feature with uniform and monolayer thickness is rarely observed. In summary, we present a synthesis to obtain monoclinic $Nb_{12}O_{29}$ NPLs with highly uniform lateral dimension and thickness that has not been reported among niobium oxides. Further, this synthesis has an advantage in terms of having low dispersion in lateral dimensions, benefiting from colloidal synthesis, while having uniform thickness that is comparable to self-assembled metal oxides.

Structural Characterization by Raman Spectroscopy. Raman spectroscopy was used to understand the structural features of the NPLs from the perspective of the Nb−O bonds, whose vibrational modes give rise to different Raman shifts
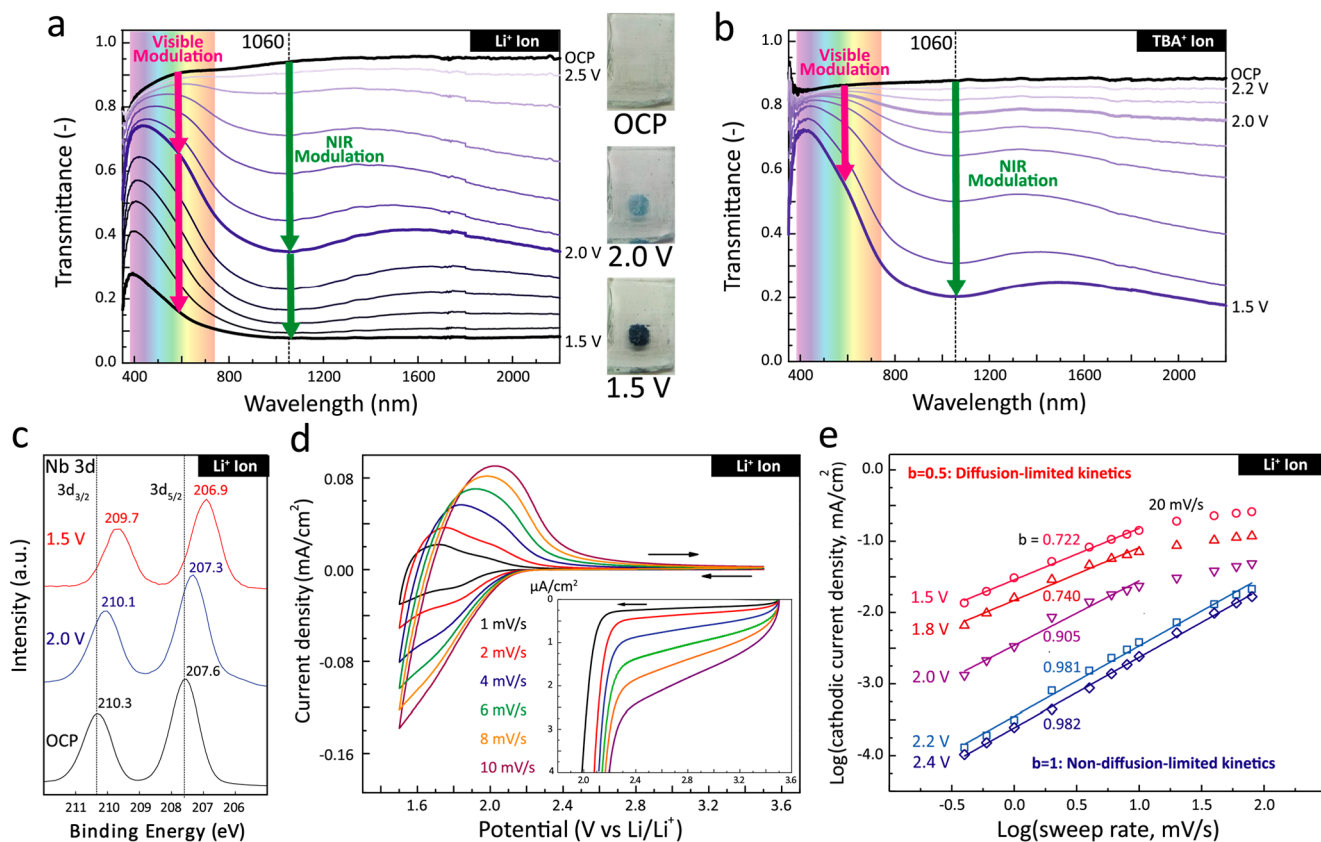
Figure 7. Spectroelectrochemical characterization of ligand-stripped NPL films with an average thickness of 350 nm. Transmittance spectra of films in (a) 1 M lithium bis(trifluoromethanesulfonyl)imide/tetraethylene glycol dimethyl ether (Li-TFSI/TG) and (b) 0.1 M tetrabutylammonium bis(trifluoromethanesulfonyl)imide (TBA-TFSI)/TG reduced at various potentials (vs Li/Li$^+$) for 5 min by chronoamperometry. Photographs of NPL films at OCP, 2.0 V, and 1.5 V in 1 M Li-TFSI/TG are presented beside (a). (c) *Ex situ* XPS spectra in the Nb 3d region of films kept at OCP or potentiostatically reduced at 2.0 and 1.5 V, respectively, in 1 M Li-TFSI/TG (vs Li/Li$^+$). (d) Cyclic voltammograms scanned between 3.5 and 1.5 V at various sweep rates in 1 M Li-TFSI/TG and the inset representing only the portion from 3.5 to 2.0 V. (e) Variation of the cathodic current density at several sweep rates for determining the *b* value of the NC films in 1 M Li-TFSI/TG.

depending on their bond orders and angles. The spectrum of NPLs has a single dominant peak at 648 cm^{-1} (Figure 6a), which is present also for bulk monoclinic Ti$_2$Nb$_{10}$O$_{29}$ crystals, an isostructural material to monoclinic Nb$_{12}$O$_{29}$.[51,52] However, the spectrum of bulk monoclinic Ti$_2$Nb$_{10}$O$_{29}$ crystals also has a strong peak at 990 cm^{-1},[51] while the spectrum of NPLs does not. We also found a peak at 990 cm^{-1} in the spectrum of bulk monoclinic Nb$_2$O$_5$ crystals, a material with similar structure, highlighting the notable absence of this peak for NPLs (Figure 6a).

The structure of Nb$_2$O$_{5-x}$ is composed mostly of vertex-shared and edge-shared NbO$_6$ octahedra, with the vertex-shared having a smaller Nb—O bond distance that corresponds to higher bond order. In Raman spectroscopy, the Nb—O bonds present in Nb$_2$O$_{5-x}$ can be classified into Nb═O terminal bonds (950−1050 cm^{-1}), Nb—O—Nb collinear bonds (800−900 cm^{-1}), Nb—O—Nb bridging bonds (550−750 cm^{-1}), ONb$_3$ bonds (350−500 cm^{-1}), and Nb—O—Nb angle deformation bonds (150−350 cm^{-1}) in a descending bond order.[31,43,53] In terms of structure, previous simulations from our groups demonstrated that the Nb═O terminal bonds and Nb—O—Nb collinear bonds are exclusively contributed by the vertex-shared NbO$_6$ octahedra, while the other three modes can be either from vertex-shared NbO$_6$ octahedra or edge-shared NbO$_6$ octahedra.[53] Therefore, the missing peak in the

Raman spectrum of NPLs is attributed to the reduced abundance of Nb═O terminal bonds due to the absence of some vertex-shared units.

Calculations of Raman spectra were used to identify the structural nature of the missing Nb—O bonds in NPLs. Several test trials of Nb$_2$O$_{5-x}$ were performed utilizing the Vienna *Ab-initio* Simulation Package (VASP), as shown in Figure S10, and discussed in the Supporting Information. First, the Raman spectrum of bulk monoclinic Nb$_{12}$O$_{29}$ crystals was generated by performing a calculation using its unit cell with periodic boundary conditions. The spectrum shows strong intensity in the Nb═O terminal bond and Nb—O—Nb collinear bond regions, which is not present in the spectrum of NPLs (Figure 6b). As discussed earlier, these two regions are exclusively contributed by vertex-shared units, thus indicating the NPLs are largely lacking vertex-shared NbO$_6$ octahedra.

Considering the NPLs are monolayer monoclinic Nb$_{12}$O$_{29}$ in the [100] direction, we performed the calculation of a cell missing several structural units in this direction. In Figure 6c, the red cell represents the unit cell of monoclinic Nb$_{12}$O$_{29}$, while the blue cell was made by stripping away the first row and last row structural units in the red cell for the purpose of simulating the potential missing structural units of NPLs in the [100] direction. As shown in Figure 6b, the calculated spectrum of the new cell demonstrates weak intensity in the

Nb=O terminal bond and Nb−O−Nb collinear bond regions, and the peak position of the Nb−O−Nb bridging bonds shifts, becoming identical to the peak of NPLs. In terms of structural units, the octahedra being stripped away are all bonded to the remaining octahedra in vertex-shared configurations (Figure 6c). Since the calculated spectrum matches the experimental spectrum of NPLs, we concluded that the reduced abundance of Nb−O bonds with higher bond order in the spectrum of NPLs could be explained by the absence of vertex-shared units. In conjunction with the monolayer thickness of NPLs, the calculated Raman spectra support a structural model of NPLs with some structural units being stripped away due to their monolayer thickness, causing the Raman spectrum to lack higher frequency peaks and the main Raman peak to shift.

Spectroelectrochemical Characterization. The ligand-capped NPLs were modified to remove the insulating OA molecules on their surface before electrochemical measurement, referred to as ligand stripping. In brief, the as-synthesized ligand-capped NPLs were treated with $NOBF_4$ to remove the OA molecules on the NC surface. Details of the ligand stripping process and thin film deposition methods are discussed in the Supporting Information and Figure S11. The average thickness of the ligand-stripped NPL films was measured using profilometry to be 350 nm. To study the mechanisms underlying an optical response to electrochemical charging, ligand-stripped NPL films were electrochemically reduced using two different cations for charge balance. Small Li^+ ions can both intercalate into the crystal lattice and be adsorbed on the surface, where they contribute to capacitance, while bulky tetrabutylammonium (TBA^+) ions must remain only at the surface.[3,54] When an NPL film is electrochemically reduced with either electrolyte, the transmittance decreases as a result of increased light absorption (Figure 7a and b). Lower potentials correspond to a larger driving force to reduce the NPL films. In Li-based electrolyte (Figure 7a), NPL films show dual-mode, sequential modulation of NIR and visible light transmission. That is, they absorb light mostly in the NIR region for potentials from open-circuit potential (OCP) to 2.0 V with a peak centered at 1060 nm wavelength and absorb light in both visible and NIR regions for potentials from 2.0 to 1.5 V. Photographs of the NPL films charged at various potentials show no color at OCP, a blue color at 2.0 V, and a black color at 1.5 V. In TBA-based electrolyte (Figure 7b), absorption occurs mostly in the NIR region with a peak centered at 1060 nm throughout the applied potential range.

In a previous report, the reduction of Nb-doped TiO_2 NC films using Li^+ ions for charge balance was found, depending on the applied potential, to populate the conduction band (CB) with delocalized electrons and to localize electrons in self-trapped states as polarons. The same NC films, when charged using a TBA-based electrolyte, host only delocalized electrons.[3] The population of the CB with delocalized electrons with surface adsorbed ions is a type of capacitive charging, while intercalative charging led to localized electrons in that material. In Nb-doped TiO_2 NCs, capacitive charging gives rise to optical absorption in the NIR region, and ion intercalation gives rise to absorption in the visible region.

Our hypothesis for the dual-mode modulation of NPL films in a Li-based electrolyte is that the first mode, ranging from OCP to 2.0 V, is a capacitive charging process that gives rise to absorption in the NIR region. As for the second mode, ranging from 2.0 to 1.5 V, this stage involves both ion intercalation that gives rise to absorption in the visible region and a persistence

of capacitive charging. When using TBA^+ ions for charge balance, ions are prevented from intercalating into the crystal lattice by their bulky nature, and therefore the absorption is confined mostly to the NIR region, associated with capacitive charging. To understand the nature of the electronic state during capacitive charging, we note that Cava et al. reported that monoclinic $Nb_{12}O_{29}$ made by chemical reduction from monoclinic Nb_2O_5 shows metallic conduction that may be associated with the delocalization of 4d electrons.[16] Recent simulations done by Koçer et al. also indicated that the presence of delocalized states in monoclinic $Nb_{12}O_{29}$ leads to its metallic conduction.[18] We propose that during electrochemical charging electrons can be injected into the CB as delocalized electrons to instigate the increased NIR absorption. Thus, in NPLs, we observe NIR electrochromism accompanying capacitive charging, while Li^+ ion intercalation triggers electrochromism in the visible, which we hypothesize is due to Nb^{5+} ions being reduced to Nb^{4+} ions.[55,56]

Previous studies proposed that the cavities for Li^+ ion intercalation in the monoclinic $Nb_{12}O_{29}$ are located within four vertex-shared NbO_6 units, as illustrated in Figure S12.[19,57] Based on a classification from these literature reports, we denoted these cavities as cavity II, IV, and V, whose specific electrochemical behavior remains unknown. Nevertheless, when the monoclinic $Nb_{12}O_{29}$ unit cell is repeated along the b axis, these cavities form channels that may offer preferable pathways for Li^+ ion diffusion. By contrast, repetition of the unit cell along the a axis produces no such channels (Figure S12). A similar structural configuration in monoclinic Nb_2O_5 also suggested that Li^+ ions may diffuse through cavities along the b axis, while the diffusion along the a axis is not preferred due to the absence of continuous cavities.[58] In a recent publication from Koçer et al., the Li^+ ion diffusion in niobium tungsten oxides, with similar shear structure to monoclinic $Nb_{12}O_{29}$, was shown to be effectively one-dimensional in the aforementioned empty diffusion channels paralleled to the b direction.[59] In conjunction with the anisotropic structure of NPLs, with the structure shown in Figure S13, we propose that the elongation along the b axis along with monolayer thickness in the a axis direction facilitates Li^+ ion diffusion by creating a diffusion channel for Li^+ ions. As shown in the structure, although having only a single unit cell thickness in the a axis, the NPLs still exhibit a few layers of vertex-shared NbO_6 units to accommodate the intercalation and diffusion of Li^+ ions. Additionally, we considered the characteristic time (t) of one-dimensional diffusion along the b axis ($t = \lambda_D^2/D_f$), where λ_D is the Debye screening length approximated to the length of the NPLs (95.2 nm), and the Li^+ ion diffusion coefficient (D_f) was approximated to 1.12×10^{-13} cm^2/s based on the literature value of monoclinic $AlNb_{11}O_{29}$.[60] Thus, t can be approximated as 800 s, representing an estimated time scale for one-dimensional Li^+ diffusion within the NPLs. This value also aligns with a typical time scale in an electrochemical experiment, such as cyclic voltammetry experiments at moderate scan rate (~20 mV/s). When electrochemically charging the NPLs, these ions reside in the proposed cavities and generate visible electrochromic absorption between 2.0 and 1.5 V. The proposed Li^+ ion diffusion channels present along the b axis of monoclinic $Nb_{12}O_{29}$ are similar to those along the c axis of orthorhombic Nb_2O_5 that facilitate Li^+ ion diffusion.[61] Unfortunately to our knowledge, the electrochromic properties of isotropic monoclinic $Nb_{12}O_{29}$, or even monoclinic Nb_2O_5, are scarcely reported, potentially due to
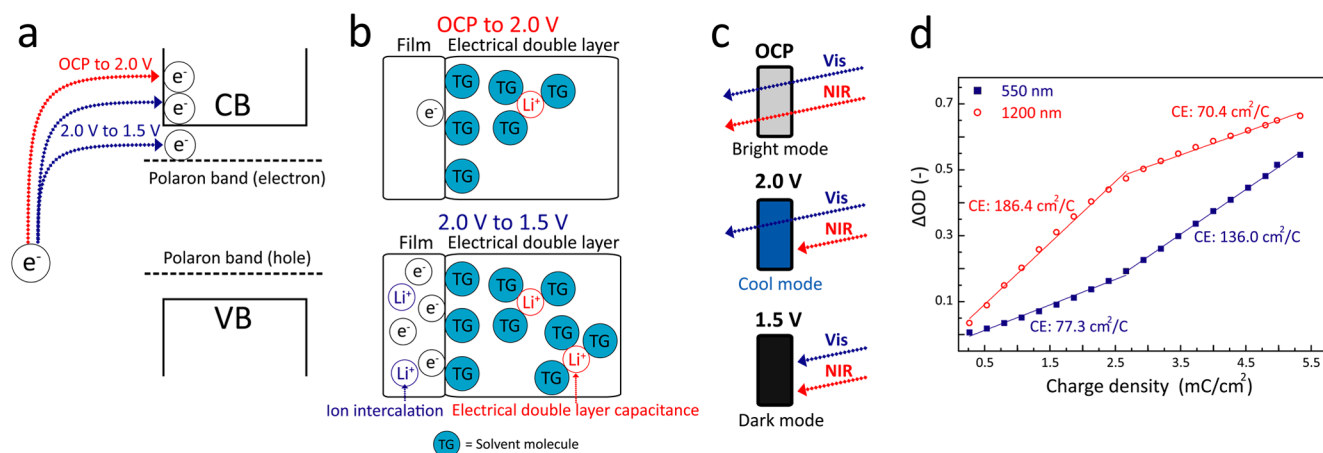
Figure 8. Schematic illustration of the electrochromic mechanism of NPL films in 1 M Li-TFSI/TG. (a) Band structure with electrons being populated into the CB as delocalized electrons (from OCP to 2.0 V) and into both the polaron band as localized electrons and CB as delocalized electrons (from 2.0 to 1.5 V). (b) Electrochemical processes showing electrical double layer capacitance in capacitive charging (from OCP to 2.0 V) and both ion intercalation and electrical double layer capacitance (from 2.0 to 1.5 V). (c) Dual-mode electrochromism of NPL films employed as smart window coatings for selectively blocking NIR light (2.0 V) and both NIR and visible light (1.5 V). (d) Variation of ΔOD against Q at 550 and 1200 nm. Films were cathodically charged at 10 $\mu A/cm^2$ using chronopotentiometry, and CE was obtained by linear fitting.

their minimum optical response, and thus a more detailed analysis of the effect of crystal structure on electrochromic properties of monoclinic $Nb_{12}O_{29}$ is not feasible at this stage.

The presence of localized electrons due to Li^+ intercalation can be investigated by observing the oxidation state of the metal ions before and after electrochemical reduction.[55] In niobium oxides specifically, Nb^{5+} reducing to Nb^{4+} during Li^+ ion intercalation should give rise to an observable decrease in the binding energy of the Nb 3d XPS peaks. XPS spectra of ligand-stripped NPL films were compared *ex situ* after electrochemical charging in Li-based electrolyte (Figure 7c). After 2.0 V applied potential, there is only a slight decrease of the binding energy compared to OCP, indicating that the reduction at 2.0 V is a capacitive charging process showing little signature of localized electrons. As for the reduction at 1.5 V, a larger shift is observed, indicating the presence of localized electrons in the NPLs. Fitting results in Figure S14 suggest 5.1% of Nb^{5+} was reduced to Nb^{4+} at 2.0 V, while at 1.5 V no clear signature of secondary peaks can be observed for extracting the ratio of Nb^{4+}/Nb^{5+}. Alternatively, based on the amount of charge injecting into the films when preparing the XPS samples, we estimated 3.9% of Nb^{5+} was reduced at 2.0 V and 30.1% of Nb^{5+} was reduced at 1.5 V. Additionally, the presence of the Li 1s peak can be clearly observed after charging at 1.5 V (Figure S15), supporting the occurrence of Li^+ ion intercalation. XPS analysis verifies that the electrochromism of NPL films from OCP to 2.0 V is dominated by capacitive charging, and the second stage from 2.0 to 1.5 V is dominated by ion intercalation accompanied by Nb^{5+} reduction.

The electrochemical response of ligand-stripped NPL films was further investigated by analyzing the dependence of current on the sweep rate in cyclic voltammograms. The so-called *b*-value test is a method for determining the extent to which the electrochemical process is limited by diffusion,[61−63] in which

$$\log(i) = \log(a) + b\log(\nu)$$

where i is the current density, ν is the sweep rate, a is a constant determined by the testing environment, and b is a constant determined by the kinetics of the electrochemical reaction. A b value of 0.5 indicates a purely diffusion-limited reaction controlled by the boundary condition of semi-infinite linear diffusion, and a b value of 1 indicates that the reaction behaves similarly to a capacitor, equivalent to a non-diffusion-limited reaction with no apparent concentration gradient in the system.

In a Li-based electrolyte, we expected that the diffusion of Li^+ ions in the crystal lattice during ion intercalation might limit the reaction kinetics. As discussed, we proposed that the Li^+ ion diffusion will follow one-dimensional channels along the long direction of NPLs, which is also the b axis of monoclinic $Nb_{12}O_{29}$, and therefore the concentration gradient building up in these channels could be limiting the reaction kinetics to show a diffusion-limited mechanism. Cyclic voltammograms of the NPL films at various sweep rate ranging from 1 to 80 mV/s were recorded, with 1 to 10 mV/s scans shown in Figure 7d, where the inset highlights the portion from 3.5 to 2.0 V. The current density includes both the charging of the electrical double layer, including Li^+ ion adsorption, and the redox reaction accompanying Li^+ ion intercalation. Intercalation dominates the cathodic current density at potentials lower than 2 V and the corresponding anodic current density when scanning from 1.5 to 3.5 V. The values of b at various potentials were obtained by linear fitting the cathodic current density dependence on scan rate (Figure 7e). At 2.2 and 2.4 V, b values are close to 1, indicating non-diffusion-limited kinetics. At lower potentials (2.0, 1.8, and 1.5 V), b values start decreasing and become lower with the decreasing potential, indicating that the kinetics are increasingly limited by diffusion of Li^+ ions. For sweep rates higher than 20 mV/s, strong polarization saturates the current density and causes deviations in the fitting results.[61] The result of the rate analysis (Figure 7e) support the electrochemical mechanisms of sequential capacitive charging and ion intercalation described above. At moderate potentials, Li^+ ions are only adsorbed on the surface of NPLs, contributing

to electrical double layer capacitance. This first stage of electrochemical charging has non-diffusion-limited kinetics with no apparent concentration gradient of Li^+ ions in the crystal lattice. At potentials below about 2.0 V, the b value starts to deviate from 1. In this stage of charging, Li^+ ions are adsorbed and also intercalate into the crystal lattice. At this stage, the kinetics will be influenced by a concentration gradient of Li^+ ions in the NPL lattice, so the rate analysis reveals the kinetics to be limited by the diffusion of Li^+ ions to some extent.

As a counterpoint, Costentin $et\ al.$ have discussed extensively the interpretation of b-value analysis.[64−66] It was shown that, in porous electrodes, ohmic drop from the charging of the pores should be the dominating factor instead of diffusion of ions in the electrolyte solution. The ohmic drop in pores, following a simple RC circuit model, can give rise to electrochemical signatures similar to that of semi-infinite diffusion with b value close to 0.5.[65] These studies have provided another aspect of interpreting the b-value analysis; that is, the diffusion-limited kinetics derived from b-value analysis could involve both the diffusion of ions in the active material and the charging of the pores. In NPL films, we have shown evidence of Li^+ ion intercalation, both in its optical effect triggering visible absorption (Figure 7a) and its chemical effect reducing Nb^{5+} ions (Figure 7c), which suggests the decrease of the b value at potentials lower than 2.0 V is the result of Li^+ ion diffusion. Potentially, the influence from the ohmic drop in pores could be investigated by varying the concentration of Li^+ ions in the electrolyte to change the electrolyte resistivity, which influences the rate of RC charging in the pores without strongly affecting the Li^+ ion diffusion rate in films.[65]

The electrochemical response of the NPLs and electronic and optical effects are illustrated in Figure 8. From OCP to 2.0 V, delocalized electrons are added to the CB of NPLs (Figure 8a), while Li^+ or TBA^+ ions are adsorbed to compensate the electronic charge, giving rise to electrical double layer capacitance (Figure 8b). From 2.0 to 1.5 V, added electrons occupy the CB as delocalized electrons and, only for a Li-based electrolyte, a polaron band as localized electrons (Figure 8a). Meanwhile, the Li^+ ions are both adsorbed on the surface and intercalated into the NC lattice (Figure 8b). In terms of the optical modulation, the NPL films can selectively block NIR light at 2.0 V with most of the visible light transmitted, while the films block both NIR and visible light at 1.5 V due to the rise of ion intercalation-induced polaronic electrochromism (Figure 8c). The dual-mode electrochromism of the NPL films was quantified by measuring their coloration efficiency (CE), defined as the ratio of optical density change at a given wavelength (ΔOD) to the charge density (Q) injected into the films (CE = $\Delta OD/Q$). In the capacitive charging regime, a higher CE was observed in the NIR (186.4 cm^2/C at 1200 nm) compared to the CE in the visible (77.3 cm^2/C at 550 nm), corresponding to the capacitive charging process with dominant absorption in the NIR region (Figure 8d). In the second stage of charging, when ion intercalation dominates, the CE in the visible (136.0 cm^2/C at 550 nm) is higher than that in the NIR (70.4 cm^2/C at 1200 nm), consistent with polaronic coloration residing primarily in the visible.

The electrochromic properties of the NPLs are distinct from other phases and morphologies of niobium oxide and may be advantageous compared to other metal oxides for particular applications. The CEs of NPLs are compared to literature values of relevant metal oxides in Table S1.[26,67−69] First, the

NPLs are the only materials that can selectively modulate visible and NIR transmission among niobium oxides. NPLs also present a much higher CE in the visible region, true for both first and second stages (77/136 cm^2/C, respectively), compared to bulk niobium oxide electrochromic films (27 cm^2/C).[67] Specifically in the NIR region, NPLs also show higher CE in the first stage (186 cm^2/C) compared to orthorhombic Nb_2O_5 NRs (76 cm^2/C), and a comparable CE value in the second stage.[26] Further, we compared the CE of NPLs with the two known dual-mode electrochromics, doped TiO_2 and $WO_{3−x}$ NCs. As discussed earlier, NPLs have a distinct two-stage coloration that can be selectively activated by the potential applied. In doped TiO_2 and $WO_{3−x}$ NCs, such tunability has not been reported potentially owing to their higher reduction potential, which instigates the visible coloration far before the saturation of NIR coloration. Thus, a parameter referred to as coloration selectivity (CE in the visible region/CE in the NIR region) was calculated to quantify this aspect of the electrochromic response. As seen in Table S1, NPLs show higher CE in the visible region for both stages compared to doped TiO_2 NCs (33.2 cm^2/C), while having a higher CE for the first stage and a lower CE for the second stage in the NIR region compared to doped TiO_2 NCs (124.5 cm^2/C). Compared to $WO_{3−x}$ NCs, two of the CE values of NPLs are higher or comparable (second visible absorption and first NIR absorption), while the other two are lower. In terms of spectral control, NPLs offer a large variation in selectivity depending on the potential applied, which is not available in doped TiO_2 and $WO_{3−x}$ NCs. This property of the NPLs may be advantageous for dual-mode electrochromic windows that require spectrally selective attenuation, such as maximizing daylighting without undue solar heat gain. In this regard, integrated solar transmittance in different spectral ranges was calculated (T_{VIS}, T_{NIR}, and T_{SOL}) with details shown in the Supporting Information and results summarized in Table S2.[4] When the NPL films are capacitively charged, at 2.0 V, T_{VIS} is high (0.65), which is beneficial for daylighting, while the T_{NIR} is relatively low (0.4), which reduces solar heat gain due to NIR insolation. At 1.5 V, low values for both T_{VIS} (0.18) and T_{NIR} (0.08) indicate a useful state for limiting both visible glare and solar heat gain. Finally, the stability of the NPL films was preliminarily tested by continuously cycling between potential steps at 4 and 1.7 V (Figure S16), showing reasonable stability with 68% of the original charge density (Q/Q_o) retained in the films after 500 cycles.

CONCLUSIONS

We developed a colloidal synthesis for phase-pure anisotropic monoclinic $Nb_{12}O_{29}$ NPLs by preparing a niobium oxo cluster as a precursor for hot injection. To prepare the precursor, $NbCl_5$ and OA were mixed, forming a complex of niobium chloro oleate that was heated to cleave the Nb−Cl bonds to form niobium oxo clusters. NC growth was tracked by an aliquot study, showing the selective growth of NPLs using the niobium oxo cluster precursor, while NRs were produced using niobium chloro oleate. NPLs were confirmed to be monolayer monoclinic $Nb_{12}O_{29}$, thin in the [100] direction and extended along the b and c directions based on AFM and XRD analysis. The monolayer feature also leads to reduced abundance of Nb−O bonds with higher bond order, as revealed by Raman spectroscopy and calculated spectra. NPL films demonstrate dual-mode electrochromism with two different electrochemical charging processes giving rise to distinct, sequential optical

responses. The first charging regime causes reduced transmission of NIR light and is found to consist of capacitive charging that generates delocalized electrons. The second charging regime brings the onset of visible absorption due to ion intercalation that generates localized electrons. Electrochemical kinetics of the films were investigated by the *b*-value test, showing that the capacitive charging process is non-diffusion-limited, while the ion intercalation process is limited by the diffusion of Li$^+$ ions in the crystal lattice. Our understanding of the electrochemical response is further supported by the observation of reduced niobium ions in the XPS spectra following ion intercalation. By establishing the principles underlying the electrochromic response of these phase-pure monoclinic Nb$_{12}$O$_{29}$ NPLs we have advanced the understanding of niobium oxides and helped lay the foundation for further electrochemical applications, particularly of nanoscale Nb$_2$O$_{5-x}$ materials.

METHODS

Materials. Toluene (>99.5%), hexane (>99%), isopropanol (>99.5%), acetone (>99.5%), *N*,*N*-dimethylformamide (DMF, anhydrous 99.8%), nitrosonium tetrafluoroborate (NOBF$_4$, 95%), tetrabutylammonium bis(trifluoromethanesulfonyl)imide (TBA-TFSI, >99.0%), oleic acid (OA, 90%), niobium chloride (NbCl$_5$, anhydrous, 99.995%), niobium ethoxide (99.95%), tetraethylene glycol dimethyl ether (TG, >99%), 1-octadecene (ODE, 90%), and chloroform-*d* (CDCl$_3$, 99.96 atom % D) were purchased from Sigma-Aldrich. Oleylamine (OM, 90%) was purchased from Acros Organics. Lithium bis(trifluoromethanesulfonyl)imide (Li-TFSI, HQ-115) was purchased from 3M. OA and OM were heated under vacuum at 120 °C before use.

NC Synthesis. All reactions were carried out using standard Schlenk line techniques under a N$_2$ atmosphere. In a typical NPL synthesis, 0.405 g of NbCl$_5$ and 4.237 g of OA were mixed in a three-neck flask in a N$_2$ glovebox and transferred to a Schlenk line. The mixture was first heated at 40 °C under vacuum for 30 min to obtain a homogeneous precursor solution with blood-red color (denoted NbP-40). Subsequently, the mixture was heated to 120 °C under vacuum for 30 min to produce the precursor solution denoted as NbP-120. While heating, the blood-red color disappeared and the resulting solution was orange. Meanwhile, the reaction flask was prepared by mixing 11.298 g of OA and 2.140 g of OM in another three-neck flask and heating to 120 °C for 30 min under vacuum, then to 300 °C under N$_2$. Once the reaction in the precursor flask was finished and switched to N$_2$ purging, NbP-120 was injected into the second flask and reacted at 300 °C for 10 min. Afterward, the solution containing NPLs was cooled to room temperature and washed using toluene as solvent for dispersion and isopropanol as antisolvent for flocculation three times. Finally, NPLs were dispersed in toluene at a concentration of 15 mg/mL. This product is referred to as a ligand-capped NPL dispersion and was used for all the characterization unless otherwise specified. Synthesis producing a mixture of NPLs and NRs was performed using the same protocol, but injecting NbP-40 precursor solution instead of NbP-120 into the reaction flask. Aliquots for tracking the NC growth were collected at 2, 4, 6, 8, and 10 min after the injection, quenched in toluene, and washed as the original NC synthesis. For comparison, niobium ethoxide precursors were prepared using the same protocol as NbP-40 and NbP-120. The synthesis producing NRs was performed following the previously reported heat-up method.[26]

Electron Microscopy. NC dispersions were dropped onto carbon-coated 400 mesh copper grids (TedPella) and dried under vacuum for analysis. Scanning electron microscopy (SEM) imaging and STEM imaging were performed using a Hitachi S5500 microscope. HRTEM imaging was performed using a JEOL 2010F microscope at 200 kV accelerating voltage.

Atomic Force Microscopy. A ligand-capped NPL dispersion was diluted to 15 µg/mL, and 10 µL of the diluted dispersion was drop-

cast on a silicon substrate. Measurement was carried out using an Asylum Research MFP-3D AFM in tapping mode.

Ultraviolet–Visible–Near-Infrared Spectroscopy. UV–vis–NIR spectra of the niobium precursors diluted in hexane (1:50 volume ratio) were measured using an Agilent Cary series UV/vis–NIR spectrophotometer.

Fourier Transform Infrared Spectroscopy. IR spectra were measured using a Bruker Vertex 70 FTIR at 4 cm^{-1} resolution. Samples of OA and niobium precursors were drop-cast on CaF$_2$ windows, and samples of NPLs were drop-cast on silicon substrates and dried.

^{1}H NMR Spectroscopy. Niobium precursor was diluted in CDCl$_3$ in special screw-capped NMR tubes (Norell) in a N$_2$ glovebox. ^{1}H NMR spectra were obtained in an Agilent/Varian MR-400 spectrometer operating at a field strength of 400 MHz.

Dynamic Light Scattering. Niobium precursor was diluted to 1 mg/mL in oleic acid for determining its particle diameter by DLS. Three consecutive measurements were performed using a Malvern Zetasizer Nano ZS.

X-ray Diffraction Measurement. An NC dispersion was dried, dispersed in mineral oil, and mounted on a cryoloop for analysis. XRD patterns were collected using a Rigaku R-Axis Spider with Cu Kα radiation with a wavelength of 1.54 Å.

X-ray Diffraction Simulation. The crystallographic information file of monoclinic Nb$_{12}$O$_{29}$ documented by Waldron *et al.* was used in simulations.[17] XRD patterns of finite crystals were simulated based on the Debye scattering formula, in which[45]

$$I(q) = \sum_i \sum_j f_i f_j \frac{\sin(q r_{ij})}{q r_{ij}}$$

where *I* is the scattering intensity, *q* ($q = 4\pi \sin \theta / \lambda$) is the scattering vector, λ (1.54 Å) is the wavelength of the X-ray, θ is the diffraction half-angle, *i* and *j* stand for the ions in finite crystals that scatter X-rays, r_{ij} is the distance between ions *i* and *j*, and f_i and f_j are the scattering factors calculated from the tabulated Cromer–Mann coefficients.[70]

A 3D crystal visualization program was used to obtain the positions of ions in finite crystals,[71] and the scattering intensity was calculated based on the scattering from all individual pairs of ions using the above equation. To simulate the experimentally observed anisotropic crystal morphology, the unit cell was repeated a variable number of times along each of the three crystallographic directions, and the resulting finite crystals were named as $\{a \times b \times c\}$. For instance, the unit cell of monoclinic Nb$_{12}$O$_{29}$ was named as $\{1 \times 1 \times 1\}$, and a supercell extended 2 times in the [100] direction (or along the *a* axis), 2 times in the [010] direction (or along the *b* axis), and 1 time in the [001] direction (or along the *c* axis) was named as $\{2 \times 2 \times 1\}$.

Raman Spectroscopy Measurement. NC dispersions were drop-cast on glass slides and dried for analysis. Spectra were collected using a Horiba LabRAM Aramis instrument using a 50× microscope objective and a laser with a 532 nm wavelength.

Raman Spectroscopy Calculations. Raman spectra were calculated using VASP.[72,73] Geometry optimization was performed with the Perdew–Burke–Ernzerhof functional with an on-site Hubbard correction on niobium using the simplified rotationally invariant approach in VASP.[74,75] The Raman spectra of the optimized structures were calculated from the derivatives of the polarizability along each normal mode.[53] The following structures taken from the Materials project were used for the calculations: Nb$_{12}$O$_{29}$ (mp-510554), Nb$_2$O$_5$ (mp-776896), Nb$_2$O$_5$ (mp-604), and Nb$_2$O$_5$ (mp-1101660).[76]

Spectroelectrochemical Measurement. Electrochemical and *in situ* optical properties of the NPL films on FTO glass substrates (70 Ω/sq) were measured in an argon glovebox using a Biologic VMP3 potentiostat and an ASD Quality Spec Pro spectrometer. Typical measurements were made in a homemade two-electrode cell consisting of an NPL film as working electrode, a Li foil serving as both the counter and reference electrode, and 1 M Li-TFSI in TG as electrolyte (1 M Li-TFSI/TG). Measurements using TBA$^+$ ions were

conducted in a homemade three-electrode cell made up of an NPL film as the working electrode, a Pt foil as the counter electrode, a commercial fritted Ag/Ag⁺ cell as the reference electrode, and 0.1 M TBA-TFSI in TG as the electrolyte (0.1 M TBA-TFSI/TG). The potentials (*vs* Ag/Ag⁺) measured in the three-electrode cell were converted to the potentials (*vs* Li/Li⁺) in the two-electrode cell by calibrating these two cells using the same NPL film. Upon dipping the NC film into the electrolytes, open-circuit potentials of 2.6 V (*vs* Li/Li⁺) and −1.0 V (*vs* Ag/Ag⁺) were recorded, respectively.

X-ray Photoelectron Spectroscopy. Samples of niobium precursors were washed with acetone, dried, and drop-cast on silicon substrates for measurement. NPL films on FTO glass were immersed in 1 M Li-TFSI/TG, followed by applying specified potentials for 5 min to reduce the films. After that, samples were transferred without air exposure *via* an argon-filled capsule to the vacuum chamber for analysis. Spectra were collected using a Kratos Axis Ultra DLD spectrometer with a monochromatic Al Kα source (1486.6 eV). The binding energy of the spectra were referenced to the C 1s peak at 284.8 eV.

ASSOCIATED CONTENT

ⓢ Supporting Information

The Supporting Information is available free of charge at https://pubs.acs.org/doi/10.1021/acsnano.0c03283.

> Details of the synthesis of bulk monoclinic Nb_2O_5 crystals, ligand-stripping method, thin film deposition; crystal structure of monoclinic $Nb_{12}O_{29}$, NPL size distribution histogram, additional AFM topographic image of NPLs, NR size distribution histogram, photograph of NR dispersion, additional XRD patterns, additional Raman spectra, aliquot study for NRs using STEM imaging, XRD patterns, and Raman spectra; figures of ligand-stripping process, additional XPS spectra, schematic illustration of intercalation mechanism and Li⁺ ion diffusion channels in NPLs, and stability measurements; table comparing the CE of electrochromic metal oxides; discussion of building Raman calculations and the influence of ligand-stripping; equation and table for integrated solar transmittance (PDF)

AUTHOR INFORMATION

Corresponding Author

Delia J. Milliron − *McKetta Department of Chemical Engineering, The University of Texas at Austin, Austin, Texas 78712-1589, United States;* ⓞ orcid.org/0000-0002-8737-451X; Email: milliron@che.utexas.edu

Authors

Hsin-Che Lu − *McKetta Department of Chemical Engineering, The University of Texas at Austin, Austin, Texas 78712-1589, United States;* ⓞ orcid.org/0000-0001-5673-2647

Sandeep Ghosh − *McKetta Department of Chemical Engineering, The University of Texas at Austin, Austin, Texas 78712-1589, United States;* ⓞ orcid.org/0000-0002-1149-9199

Naman Katyal − *Department of Chemistry and the Oden Institute for Computational Engineering and Sciences, The University of Texas at Austin, Austin, Texas 78712-0165, United States*

Vikram S. Lakhanpal − *McKetta Department of Chemical Engineering, The University of Texas at Austin, Austin, Texas 78712-1589, United States*

Ioana R. Gearba-Dolocan − *Texas Materials Institute, The University of Texas at Austin, Austin, Texas 78712, United States*

Graeme Henkelman − *Department of Chemistry and the Oden Institute for Computational Engineering and Sciences, The University of Texas at Austin, Austin, Texas 78712-0165, United States;* ⓞ orcid.org/0000-0002-0336-7153

Complete contact information is available at:
https://pubs.acs.org/10.1021/acsnano.0c03283

Author Contributions

§S. Ghosh and N. Katyal contributed equally to this work.

Notes

The authors declare the following competing financial interest(s): D.J.M. has a financial interest in Heliotrope Technologies, a company pursuing commercial development of electrochromic devices.

REFERENCES

(1) Wang, Y.; Runnerstrom, E. L.; Milliron, D. J. Switchable Materials for Smart Windows. *Annu. Rev. Chem. Biomol. Eng.* **2016**, 7, 283−304.

(2) Runnerstrom, E. L.; Llordés, A.; Lounis, S. D.; Milliron, D. J. Nanostructured Electrochromic Smart Windows: Traditional Materials and NIR-Selective Plasmonic Nanocrystals. *Chem. Commun.* **2014**, 50, 10555−10572.

(3) Dahlman, C. J.; Tan, Y.; Marcus, M. A.; Milliron, D. J. Spectroelectrochemical Signatures of Capacitive Charging and Ion Insertion in Doped Anatase Titania Nanocrystals. *J. Am. Chem. Soc.* **2015**, 137, 9160−9166.

(4) Kim, J.; Ong, G. K.; Wang, Y.; LeBlanc, G.; Williams, T. E.; Mattox, T. M.; Helms, B. A.; Milliron, D. J. Nanocomposite Architecture for Rapid, Spectrally-Selective Electrochromic Modulation of Solar Transmittance. *Nano Lett.* **2015**, 15, 5574−5579.

(5) Heo, S.; Kim, J.; Ong, G. K.; Milliron, D. J. Template-Free Mesoporous Electrochromic Films on Flexible Substrates from Tungsten Oxide Nanorods. *Nano Lett.* **2017**, 17, 5756−5761.

(6) Barawi, M.; De Trizio, L.; Giannuzzi, R.; Veramonti, G.; Manna, L.; Manca, M. Dual Band Electrochromic Devices Based on Nb-Doped TiO₂ Nanocrystalline Electrodes. *ACS Nano* **2017**, 11, 3576−3584.

(7) Balaji, S.; Djaoued, Y.; Albert, A.-S.; Ferguson, R. Z.; Brüning, R. Hexagonal Tungsten Oxide Based Electrochromic Devices: Spectroscopic Evidence for the Li Ion Occupancy of Four-Coordinated Square Windows. *Chem. Mater.* **2009**, 21, 1381−1389.

(8) Wang, Y.; Kim, J.; Gao, Z.; Zandi, O.; Heo, S.; Banerjee, P.; Milliron, D. J. Disentangling Photochromism and Electrochromism by Blocking Hole Transfer at the Electrolyte Interface. *Chem. Mater.* **2016**, 28, 7198−7202.

(9) Nowak, I.; Ziolek, M. Niobium Compounds: Preparation, Characterization, and Application in Heterogeneous Catalysis. *Chem. Rev.* **1999**, 99, 3603−3624.

(10) Rani, R. A.; Zoolfakar, A. S.; O'Mullane, A. P.; Austin, M. W.; Kalantar-Zadeh, K. Thin Films and Nanostructures of Niobium Pentoxide: Fundamental Properties, Synthesis Methods and Applications. *J. Mater. Chem. A* **2014**, *2*, 15683−15703.

(11) Yoshimura, K.; Miki, T.; Iwama, S.; Tanemura, S. Characterization of Niobium Oxide Electrochromic Thin Films Prepared by Reactive D.C. Magnetron Sputtering. *Thin Solid Films* **1996**, *281−282*, 235−238.

(12) Schmitt, M.; Heusing, S.; Aegerter, M. A.; Pawlicka, A.; Avellaneda, C. Electrochromic Properties of Nb_2O_5 Sol-Gel Coatings. *Sol. Energy Mater. Sol. Cells* **1998**, *54*, 9−17.

(13) Mjejri, I.; Grocassan, R.; Rougier, A. Enhanced Coloration for Hybrid Niobium-Based Electrochromic Devices. *ACS Appl. Energy Mater.* **2018**, *1*, 4359−4366.

(14) Kumagai, N.; Koishikawa, Y.; Komaba, S.; Koshiba, N. Thermodynamics and Kinetics of Lithium Intercalation into Nb_2O_5 Electrodes for a 2 V Rechargeable Lithium Battery. *J. Electrochem. Soc.* **1999**, *146*, 3203−3210.

(15) Le Viet, A.; Jose, R.; Reddy, M. V.; Chowdari, B. V. R.; Ramakrishna, S. Nb_2O_5 Photoelectrodes for Dye-Sensitized Solar Cells: Choice of the Polymorph. *J. Phys. Chem. C* **2010**, *114*, 21795−21800.

(16) Cava, R. J.; Batlogg, B.; Krajewski, J. J.; Poulsen, H. F.; Gammel, P.; Peck, W. F.; Rupp, L. W. Electrical and Magnetic Properties of $Nb_2O_{5-\delta}$ Crystallographic Shear Structures. *Phys. Rev. B: Condens. Matter Mater. Phys.* **1991**, *44*, 6973−6981.

(17) Waldron, J. E. L.; Green, M. A.; Neumann, D. A. Charge and Spin Ordering in Monoclinic $Nb_{12}O_{29}$. *J. Am. Chem. Soc.* **2001**, *123*, 5833−5834.

(18) Koçer, C. P.; Griffith, K. J.; Grey, C. P.; Morris, A. J. First-Principles Study of Localized and Delocalized Electronic States in Crystallographic Shear Phases of Niobium Oxide. *Phys. Rev. B: Condens. Matter Mater. Phys.* **2019**, *99*, 075151.

(19) Li, Y.; Sun, C.; Goodenough, J. B. Electrochemical Lithium Intercalation in Monoclinic $Nb_{12}O_{29}$. *Chem. Mater.* **2011**, *23*, 2292−2294.

(20) Özer, N.; Chen, D.-G.; Lampert, C. M. Preparation and Properties of Spin-Coated Nb_2O_5 Films by the Sol-Gel Process for Electrochromic Applications. *Thin Solid Films* **1996**, *277*, 162−168.

(21) Ali, R. F.; Nazemi, A. H.; Gates, B. D. Surfactant Controlled Growth of Niobium Oxide Nanorods. *Cryst. Growth Des.* **2017**, *17*, 4637−4646.

(22) Lopes, O. F.; Paris, E. C.; Ribeiro, C. Synthesis of Nb_2O_5 Nanoparticles through the Oxidant Peroxide Method Applied to Organic Pollutant Photodegradation: A Mechanistic Study. *Appl. Catal., B* **2014**, *144*, 800−808.

(23) Masse, J. P.; Szymanowski, H.; Zabeida, O.; Amassian, A.; Klemberg-Sapieha, J. E.; Martinu, L. Stability and Effect of Annealing on the Optical Properties of Plasma-Deposited Ta_2O_5 and Nb_2O_5 films. *Thin Solid Films* **2006**, *515*, 1674−1682.

(24) Cheng, J. G.; Zhou, J. S.; Goodenough, J. B.; Zhou, H. D.; Wiebe, C. R.; Takami, T.; Fujii, T. Spin Fluctuations in the Antiferromagnetic Metal $Nb_{12}O_{29}$. *Phys. Rev. B: Condens. Matter Mater. Phys.* **2009**, *80*, 134428.

(25) Agrawal, A.; Cho, S. H.; Zandi, O.; Ghosh, S.; Johns, R. W.; Milliron, D. J. Localized Surface Plasmon Resonance in Semiconductor Nanocrystals. *Chem. Rev.* **2018**, *118*, 3121−3207.

(26) Ong, G. K.; Saez Cabezas, C. A.; Dominguez, M. N.; Skjærvø, S. L.; Heo, S.; Milliron, D. J. Electrochromic Niobium Oxide Nanorods. *Chem. Mater.* **2020**, *32*, 468−475.

(27) Weissman, J. G.; Ko, E. I.; Wynblatt, P.; Howe, J. M. High-Resolution Electron Microscopy and Image Simulation of TT-,T-, and H-Niobia and Model Silica-Supported Niobium Surface Oxides. *Chem. Mater.* **1989**, *1*, 187−193.

(28) Andersen, E. N.; Klimczuk, T.; Miller, V. L.; Zandbergen, H. W.; Cava, R. J. Nanometer Structural Columns and Frustration of Magnetic Ordering in $Nb_{12}O_{29}$. *Phys. Rev. B: Condens. Matter Mater. Phys.* **2005**, *72*, 033413.

(29) Marchetti, F.; Pampaloni, G.; Zacchini, S. The Chemistry of Niobium and Tantalum Halides, MX_5, with Haloacetic Acids and Their Related Anhydrides: Anhydride C-H Bond Activation Promoted by MF_5. *Polyhedron* **2008**, *27*, 1969−1976.

(30) Den Auwer, C.; Andrews, M.; Briois, V.; Cartier dit Moulin, C.; Dexpert, H. New Synthetic Route to Rare Earth Doped Halide Clusters. *J. Chim. Phys. Phys.-Chim. Biol.* **1995**, *92*, 1084−1092.

(31) Orel, B.; Maček, M.; Grdadolnik, J.; Meden, A. *In Situ* UV-Vis and *Ex Situ* IR Spectroelectrochemical Investigations of Amorphous and Crystalline Electrochromic Nb_2O_5 Films in Charged/Discharged States. *J. Solid State Electrochem.* **1998**, *2*, 221−236.

(32) Buonsanti, R.; Grillo, V.; Carlino, E.; Giannini, C.; Kipp, T.; Cingolani, R.; Cozzoli, P. D. Nonhydrolytic Synthesis of High-Quality Anisotropically Shaped Brookite TiO_2 Nanocrystals. *J. Am. Chem. Soc.* **2008**, *130*, 11223−11233.

(33) Bronstein, L. M.; Huang, X.; Retrum, J.; Schmucker, A.; Pink, M.; Stein, B. D.; Dragnea, B. Influence of Iron Oleate Complex Structure on Iron Oxide Nanoparticle Formation. *Chem. Mater.* **2007**, *19*, 3624−3632.

(34) Cho, S. H.; Ghosh, S.; Berkson, Z. J.; Hachtel, J. A.; Shi, J.; Zhao, X.; Reimnitz, L. C.; Dahlman, C. J.; Ho, Y.; Yang, A.; Liu, Y.; Idrobo, J.-C.; Chmelka, B. F.; Milliron, D. J. Syntheses of Colloidal $F:In_2O_3$ Cubes: Fluorine-Induced Faceting and Infrared Plasmonic Response. *Chem. Mater.* **2019**, *31*, 2661−2676.

(35) Nakamoto, K. Applications in Coordination Chemistry. In *Infrared and Raman Spectra of Inorganic and Coordination Compounds: Part B: Applications in Coordination, Organometallic, and Bioinorganic Chemistry*, 6th ed.; John Wiley & Sons, Inc.: Hoboken, NJ, 2008; pp 64−67.

(36) Hens, Z.; Martins, J. C. A Solution NMR Toolbox for Characterizing the Surface Chemistry of Colloidal Nanocrystals. *Chem. Mater.* **2013**, *25*, 1211−1221.

(37) Spectral Database for Organic Compounds (SDBS); infrared spectrum; SDBS No. 17181; RN 112-77-6. IR spectrum; SDBS No. 19203; RN 24909-72-6. ¹H NMR; SDBS No. 1035; RN 112-80-1. ¹H NMR; SDBS No. 17181; RN 112-77-6. ¹H NMR; SDBS No. 7846; 638-08-4. http://riodb01.ibase.aist.go.jp/sdbs/ (accessed June 22, 2020).

(38) Hu, W.; Zhao, Y.; Liu, Z.; Zhu, Y. NbS_2/Nb_2O_5 Nanocables. *Nanotechnology* **2007**, *18*, 095605.

(39) Zhang, H.; Wang, Y.; Yang, D.; Li, Y.; Liu, H.; Liu, P.; Wood, B. J.; Zhao, H. Directly Hydrothermal Growth of Single Crystal $Nb_3O_7(OH)$ Nanorod Film for High Performance Dye-Sensitized Solar Cells. *Adv. Mater.* **2012**, *24*, 1598−1603.

(40) Ghosh, S.; Manna, L. The Many "Facets" of Halide Ions in the Chemistry of Colloidal Inorganic Nanocrystals. *Chem. Rev.* **2018**, *118*, 7804−7864.

(41) Gordon, T. R.; Cargnello, M.; Paik, T.; Mangolini, F.; Weber, R. T.; Fornasiero, P.; Murray, C. B. Nonaqueous Synthesis of TiO_2 Nanocrystals Using TiF_4 to Engineer Morphology, Oxygen Vacancy Concentration, and Photocatalytic Activity. *J. Am. Chem. Soc.* **2012**, *134*, 6751−6761.

(42) Jehng, J. M.; Wachs, I. E. Structural Chemistry and Raman Spectra of Niobium Oxides. *Chem. Mater.* **1991**, *3*, 100−107.

(43) Ikeya, T.; Senna, M. Change in the Structure of Niobium Pentoxide Due to Mechanical and Thermal Treatments. *J. Non-Cryst. Solids* **1988**, *105*, 243−250.

(44) Jehng, J.-M.; Wachs, I. E. Niobium Oxide Solution Chemistry. *J. Raman Spectrosc.* **1991**, *22*, 83−89.

(45) Murray, C. B.; Kagan, C. R.; Bawendi, M. G. Synthesis and Characterization of Monodisperse Nanocrystals and Close-Packed Nanocrystal Assemblies. *Annu. Rev. Mater. Sci.* **2000**, *30*, 545−610.

(46) Murray, C. B.; Norris, D. J.; Bawendi, M. G. Synthesis and Characterization of Nearly Monodisperse CdE (E = Sulfur, Selenium, Tellurium) Semiconductor Nanocrystallites. *J. Am. Chem. Soc.* **1993**, *115*, 8706−8715.

(47) Mei, J.; Liao, T.; Kou, L.; Sun, Z. Two-Dimensional Metal Oxide Nanomaterials for Next-Generation Rechargeable Batteries. *Adv. Mater.* **2017**, *29*, 1700176.

(48) ten Elshof, J. E.; Yuan, H.; Gonzalez Rodriguez, P. Two-Dimensional Metal Oxide and Metal Hydroxide Nanosheets: Synthesis, Controlled Assembly and Applications in Energy Conversion and Storage. *Adv. Eng. Mater.* **2016**, *6*, 1600355.

(49) Sun, Z.; Liao, T.; Dou, Y.; Hwang, S. M.; Park, M.-S.; Jiang, L.; Kim, J. H.; Dou, S. X. Generalized Self-Assembly of Scalable Two-Dimensional Transition Metal Oxide Nanosheets. *Nat. Commun.* **2014**, *5*, 3813.

(50) Kim, J.; Agrawal, A.; Krieg, F.; Bergerud, A.; Milliron, D. J. The Interplay of Shape and Crystalline Anisotropies in Plasmonic Semiconductor Nanocrystals. *Nano Lett.* **2016**, *16*, 3879−3884.

(51) Cheng, Q.; Liang, J.; Zhu, Y.; Si, L.; Guo, C.; Qian, Y. Bulk $Ti_2Nb_{10}O_{29}$ as Long-Life and High-Power Li-Ion Battery Anodes. *J. Mater. Chem. A* **2014**, *2*, 17258−17262.

(52) McConnell, A. A.; Aderson, J. S.; Rao, C. N. R. Raman Spectra of Niobium Oxides. *Spectrochim. Acta* **1976**, *32*, 1067−1076.

(53) Llordés, A.; Wang, Y.; Fernandez-Martinez, A.; Xiao, P.; Lee, T.; Poulain, A.; Zandi, O.; Saez Cabezas, C. A.; Henkelman, G.; Milliron, D. J. Linear Topology in Amorphous Metal Oxide Electrochromic Networks Obtained *via* Low-Temperature Solution Processing. *Nat. Mater.* **2016**, *15*, 1267.

(54) Ghosh, S.; Lu, H.-C.; Cho, S. H.; Maruvada, T.; Price, M. C.; Milliron, D. J. Colloidal ReO_3 Nanocrystals: Extra Re d-Electron Instigating a Plasmonic Response. *J. Am. Chem. Soc.* **2019**, *141*, 16331−16343.

(55) Özer, N.; Rubin, M. D.; Lampert, C. M. Optical and Electrochemical Characteristics of Niobium Oxide Films Prepared by Sol-Gel Process and Magnetron Sputtering a Comparison. *Sol. Energy Mater. Sol. Cells* **1996**, *40*, 285−296.

(56) Macek, M.; Orel, B.; Krasovec, U. O. The Effect of Lithiation on the Electrochromism of Sol-Gel Derived Niobium Oxide Films. *J. Electrochem. Soc.* **1997**, *144*, 3002−3010.

(57) Cava, R. J.; Murphy, D. W.; Zahurak, S. M. Lithium Insertion in Wadsley-Roth Phases Based on Niobium Oxide. *J. Electrochem. Soc.* **1983**, *130*, 2345−2351.

(58) Griffith, K. J.; Forse, A. C.; Griffin, J. M.; Grey, C. P. High-Rate Intercalation without Nanostructuring in Metastable Nb_2O_5 Bronze Phases. *J. Am. Chem. Soc.* **2016**, *138*, 8888−8899.

(59) Koçer, C. P.; Griffith, K. J.; Grey, C. P.; Morris, A. J. Lithium Diffusion in Niobium Tungsten Oxide Shear Structures. *Chem. Mater.* **2020**, *32*, 3980−3989.

(60) Lou, X.; Li, R.; Zhu, X.; Luo, L.; Chen, Y.; Lin, C.; Li, H.; Zhao, X. S. New Anode Material for Lithium-Ion Batteries: Aluminum Niobate ($AlNb_{11}O_{29}$). *ACS Appl. Mater. Interfaces* **2019**, *11*, 6089−6096.

(61) Augustyn, V.; Come, J.; Lowe, M. A.; Kim, J. W.; Taberna, P.-L.; Tolbert, S. H.; Abruña, H. D.; Simon, P.; Dunn, B. High-rate Electrochemical Energy Storage through Li^+ Intercalation Pseudocapacitance. *Nat. Mater.* **2013**, *12*, 518.

(62) Bard, A. J.; Faulkner, L. R. *Electrochemical Methods: Fundamentals and Applications*, 2nd ed.; John Wiley & Sons: New York, 1980.

(63) Lindström, H.; Södergren, S.; Solbrand, A.; Rensmo, H.; Hjelm, J.; Hagfeldt, A.; Lindquist, S.-E. Li^+ Ion Insertion in TiO_2 (Anatase). 2. Voltammetry on Nanoporous Films. *J. Phys. Chem. B* **1997**, *101*, 7717−7722.

(64) Costentin, C.; Porter, T. R.; Savéant, J.-M. How Do Pseudocapacitors Store Energy? Theoretical Analysis and Experimental Illustration. *ACS Appl. Mater. Interfaces* **2017**, *9*, 8649−8658.

(65) Costentin, C.; Savéant, J.-M. Electrochemical Capacitive Charging in Porous Materials. Discriminating between Ohmic Potential Drop and Counterion Diffusion. *ACS Appl. Energy Mater.* **2019**, *2*, 4981−4986.

(66) Costentin, C.; Savéant, J.-M. Energy Storage: Pseudocapacitance in Prospect. *Chem. Sci.* **2019**, *10*, 5656−5666.

(67) Heusing, S.; Sun, D. L.; Otero-Anaya, J.; Aegerter, M. A. Grey, Brown and Blue Coloring Sol-Gel Electrochromic Devices. *Thin Solid Films* **2006**, *502*, 240−245.

(68) Zhang, S.; Cao, S.; Zhang, T.; Fisher, A.; Lee, J. Y. Al^{3+} Intercalation/De-Intercalation-Enabled Dual-Band Electrochromic Smart Windows with a High Optical Modulation, Quick Response and Long Cycle Life. *Energy Environ. Sci.* **2018**, *11*, 2884−2892.

(69) Cao, S.; Zhang, S.; Zhang, T.; Lee, J. Y. Fluoride-Assisted Synthesis of Plasmonic Colloidal Ta-Doped TiO_2 Nanocrystals for Near-Infrared and Visible-Light Selective Electrochromic Modulation. *Chem. Mater.* **2018**, *30*, 4838−4846.

(70) Brown, P. J.; Fox, A. G.; Maslen, E. N.; O'Keefe, M. A.; Willis, B. T. M. *International Tables for Crystallography*; John Wiley & Sons, Ltd., 2006; Vol. *C*.

(71) Momma, K.; Izumi, F. VESTA: A Three-Dimensional Visualization System for Electronic and Structural Analysis. *J. Appl. Crystallogr.* **2008**, *41*, 653−658.

(72) Kresse, G.; Hafner, J. *Ab Initio* Molecular Dynamics for Liquid Metals. *Phys. Rev. B: Condens. Matter Mater. Phys.* **1993**, *47*, 558−561.

(73) Fonari, A.; Stauffer, S. vasp_raman.py. https://github.com/raman-sc/VASP/: 2013 (accessed June 22, 2020).

(74) Perdew, J. P.; Burke, K.; Ernzerhof, M. Generalized Gradient Approximation Made Simple. *Phys. Rev. Lett.* **1996**, *77*, 3865−3868.

(75) Dudarev, S. L.; Botton, G. A.; Savrasov, S. Y.; Humphreys, C. J.; Sutton, A. P. Electron-Energy-Loss Spectra and the Structural Stability of Nickel Oxide: An LSDA+U Study. *Phys. Rev. B: Condens. Matter Mater. Phys.* **1998**, *57*, 1505−1509.

(76) Jain, A.; Ong, S. P.; Hautier, G.; Chen, W.; Richards, W. D.; Dacek, S.; Cholia, S.; Gunter, D.; Skinner, D.; Ceder, G.; Persson, K. A. Commentary: The Materials Project: A Materials Genome Approach to Accelerating Materials Innovation. *APL Mater.* **2013**, *1*, 011002.